Geochemistry Geophysics Geosystems G3

Article
Volume 12, Number 5
25 May 2011
Q0AG03, doi:10.1029/2011GC003503
ISSN: 1525-2027

Published by AGU and the Geochemical Society

Quantitative constraint on footwall rotations at the 15°45′N oceanic core complex, Mid-Atlantic Ridge: Implications for oceanic detachment fault processes

C. J. MacLeod
School of Earth and Ocean Sciences, Cardiff University, Main Building, Park Place, Cardiff CF10 3AT, UK (macleod@cardiff.ac.uk)

J. Carlut
Département de Géologie, UMR 8538, École Normale Supérieure, 24 Rue Lhomond, F-75231 Paris CEDEX 05, France

Now at Equipe Géosciences Marines, Institut de Physique du Globe de Paris, UMR 7154, Sorbonne Paris Cité, Université Paris Diderot, CNRS, F-75005 Paris, France

J. Escartín
Equipe Géosciences Marines, Institut de Physique du Globe de Paris, UMR 7154, Sorbonne Paris Cité, Université Paris Diderot, CNRS, F-75005 Paris, France

H. Horen
Département de Géologie, JE 2532, Université de Picardie Jules Verne, 1 rue des Louvels, F-80037 Amiens, France

A. Morris
School of Geography, Earth and Environmental Sciences, University of Plymouth, Drake Circus, Plymouth PL4 8AA, UK

[1] The subsurface geometry of detachment faults at slow spreading mid-ocean ridges is debated: are they planar features that form and slip at low angles, as often inferred for their continental equivalents, or do they initiate at steep angles and then flatten in response to flexural unloading as displacement proceeds, as predicted in "rolling hinge" conceptual models? An essential difference is that significant rotation of the footwall should occur in the rolling hinge but not the planar fault model. This can be tested using paleomagnetism. Previous attempts to address this question have relied upon data from azimuthally unoriented drill cores. Although results are consistent with large rotations having occurred, these interpretations are very nonunique, and other solutions that require minimal rotations are equally permissible. We here present a rigorous analysis of paleomagnetic and structural data from a unique set of azimuthally oriented cores, collected using a seabed rock drill, from the 15°45′N oceanic core complex on the Mid-Atlantic Ridge. By considering the full paleomagnetic remanence vector in combination with kinematic data from the detachment fault shear zone we are able to quantitatively constrain the geometrically permissible axes and magnitudes of rotation of the detachment fault footwall, for the first time without having to make a priori assumptions about the orientation of the axis. We show that significant rotations (64° ± 16°) have indeed occurred, about a gently plunging, near-ridge-parallel axis, robustly supporting the rolling hinge models. We further discuss the geological implications of this result for oceanic detachment fault processes.

Components: 16,300 words, 15 figures, 1 table.

Keywords: oceanic core complex; oceanic detachment fault; tectonic rotation; footwall rotation; oriented core; seabed rock drill.

Index Terms: 8118 Tectonophysics: Dynamics and mechanics of faulting (8004); 8011 Structural Geology: Kinematics of crustal and mantle deformation; 3045 Marine Geology and Geophysics: Seafloor morphology, geology, and geophysics.

Received 4 January 2011; **Revised** 25 March 2011; **Accepted** 30 March 2011; **Published** 25 May 2011.

MacLeod, C. J., J. Carlut, J. Escartín, H. Horen, and A. Morris (2011), Quantitative constraint on footwall rotations at the 15°45′N oceanic core complex, Mid-Atlantic Ridge: Implications for oceanic detachment fault processes, *Geochem. Geophys. Geosyst.*, *12*, Q0AG03, doi:10.1029/2011GC003503.

Theme: Oceanic Detachment Faults
Guest Editors: J. P. Canales, M. Cheadle, J. Escartin, G. Fruh-Green, and B. John

1. Introduction

[2] It is now widely recognized that large-offset extensional (detachment) faulting plays a significant role in accommodating plate separation at slow spreading mid-ocean ridges: as much as 50% of the lithosphere generated at the Mid-Atlantic Ridge (MAR) between 12°30′N and 35°N may be influenced by such faults [*Escartín et al.*, 2008b]. Oceanic core complexes (OCCs), at which lower crustal and mantle rocks are exposed on the seafloor, are the uplifted footwalls of subhorizontal detachment fault surfaces. Although in many ways analogous to the metamorphic core complexes that form the footwalls of continental detachment fault systems [e.g., *John*, 1987], the origins and mode of deformation of oceanic detachments may be very different. A key parameter, and a moot point, is the subsurface geometry of oceanic detachments: are they planar features that are initiated and slip at a low dip angle, and therefore remain shallow at depth [e.g., *Karson*, 1990; *Cannat et al.*, 1997; *Lagabrielle et al.*, 1998; *Ildefonse et al.*, 2007], or are they instead curved structures that steepen progressively downward, active only on their steeply dipping portions [e.g., *Tucholke and Lin*, 1994; *Tucholke et al.*, 1998, 2008; *Smith et al.*, 2006, 2008; *MacLeod et al.*, 2009] (Figure 1)? The competing models have profoundly different views as to the origin of oceanic detachment faults, with attendant implications for their deformation mechanisms and for the behavior of the lithosphere at mid-ocean ridges as a whole.

[3] The steepening-downward geometry satisfies conventional Mohr-Coulomb theory [e.g., *Anderson*, 1951; *Byerlee*, 1978], that normal faults should be initiated at angles at ~60–70° and lock up at angles of less than ~30°; in this case flattening and rollover of the inactive, exhumed portion of the fault occurs in response to flexure at a "rolling hinge" during unloading of the hanging wall [e.g., *Buck*, 1988; *Wernicke and Axen*, 1988; *Lavier et al.*, 1999]. A low-angle subsurface geometry is, however, inferred for many continental detachment fault systems [e.g., *John and Foster*, 1993; *Abers et al.*, 1997], and there is increasing evidence that active slip may indeed occur by creep on low-angle fault surfaces [e.g., *Hreinsdottir and Bennett*, 2009; *Campani et al.*, 2010; *Lecomte et al.*, 2010], probably aided by high pore fluid pressures and/or localized deformation of weak minerals (e.g., talc [*Moore and Lockner*, 2008]) along the fault planes [e.g., *Wernicke*, 1995; *Abers*, 2009].

[4] Direct constraint on the subsurface geometry of oceanic detachments and other normal faults at slow spreading ridges is limited. Some support for a low dip angle at depth comes from seismic reflection imaging of Cretaceous crust in the Atlantic Ocean, which reveals fault surfaces that dip at 20–30°, though traced only to depths of 2 to 3.5 km into basement [*Ranero and Reston*, 1999]. The most direct evidence to date, and a potentially contrasting view, comes from a microearthquake study of the TAG area of the Mid-Atlantic Ridge (MAR) at 26°N [*deMartin et al.*, 2007]. Although the TAG area is apparently not (yet?) a fully developed, corrugated OCC, hypocenters there define a seismogenic fault plane dipping at ~70° between 3 and 7 km subseafloor, and curved in plan view with a shape mimicking that of the detachment fault exposed at the seafloor. Although no updip curvature of this seismogenic plane is observed directly, it is interpreted as connecting with an aseismic and shallow dipping (20°) fault surface at shallower levels that they infer from tomographic modeling and projection of seafloor fault geometry [*Canales et al.*, 2007; *deMartin et al.*, 2007]. A concave-downward

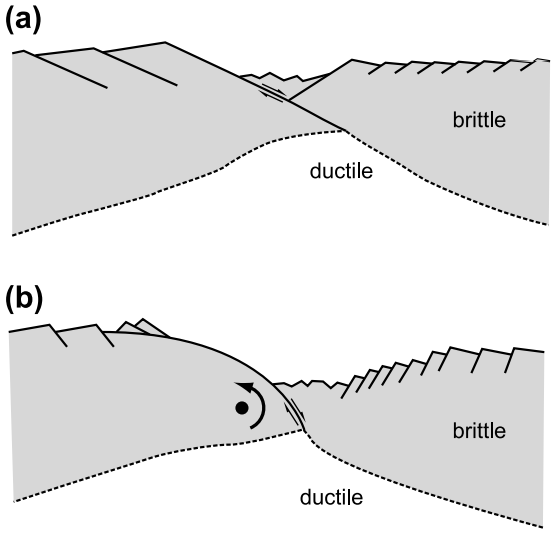

Figure 1. Cartoon illustration of the essential differences between planar and rolling hinge detachment fault models. (a) Planar models invoke a shallow subsurface geometry to the detachment fault, which is initiated and slips at a low angle. No significant tectonic rotation is implied in the detachment footwall. (b) In rolling hinge models the detachment is initiated and slips at a steep angle, flattening and becoming inactive as it is brought toward the surface in response to flexure and unloading of the footwall of the detachment. Significant rotation of the footwall occurs in consequence.

geometry to oceanic detachment faults at depth is also consistent with the observation of curved fault planes exposed at the seafloor, together with inferred rotation of seafloor blocks, in areas where the accretion of oceanic lithosphere is believed to be dominated by detachment faulting [*Smith et al.*, 2008; *MacLeod et al.*, 2009; *Schouten et al.*, 2010].

[5] There exists an essential, inherent kinematic difference between the two classes of models. In the case of planar faulting deformation should involve little or no tilting of the detachment footwall or hanging wall; in contrast, the rolling hinge models, with curved fault planes, require that significant tectonic rotation of the detachment footwall should occur as it moves outward and upward in response to flexure during exhumation [*Buck*, 1988; *Wernicke and Axen*, 1988; *Buck et al.*, 2005; *Tucholke et al.*, 2008]. This essential difference in rotational strain history should be distinguishable by means of an examination of magnetic remanence direction data from the footwalls of OCCs.

[6] In this paper we test the above models by means of a paleomagnetic and structural study of hard rock drill cores from the 15°45′N OCC on the MAR, collected using a unique robotic seabed rock drill that is able to acquire geographically oriented core. We present a new methodology for analyzing fully oriented samples, as a result of which we can for the first time independently determine both the magnitude and axis of tectonic rotation and quantify the uncertainties in each. We discuss the implications of our results from 15°45′N for oceanic detachment fault processes in general.

2. Background

2.1. Previous Paleomagnetic Constraints on Footwall Rotations at OCCs

2.1.1. Inclination-Only Data

[7] Previous attempts to document and quantify rotations at OCCs have been based upon interpretation of paleomagnetic data in Ocean Drilling Program (ODP) cores from the MAR in the vicinity of the Fifteen-Twenty fracture zone (ODP Leg 209 [*Kelemen et al.*, 2004; *Garcés and Gee*, 2007]), and Integrated Ocean Drilling Program (IODP) cores from the Atlantis Massif OCC on the MAR at 30°N (IODP Expeditions 304 and 305 [*Blackman et al.*, 2006; *Morris et al.*, 2009; *Zhao and Tominaga*, 2009]). Inclinations of stable remanences in drill sites are mostly shallower than the expected inclination of the time-averaged geocentric axial dipole (GAD) direction. Shifts in the horizontal component (declination) of the magnetic remanence direction are, however, unconstrained, as ODP and IODP cores are not oriented in azimuth. At the (N-S trending) MAR the shallower inclinations have nevertheless been interpreted as firm evidence for substantial rotations (50–80°) having occurred about horizontal, ridge-parallel axes in the Fifteen-Twenty fracture zone region [*Garcés and Gee*, 2007], and at Atlantis Massif (~50° [*Zhao and Tominaga*, 2009]), and thus taken as support for the rolling hinge detachment fault models. In marked contrast, however, at Atlantis Bank, adjacent to the (E-W trending) SW Indian Ridge, the shallower inclinations are consistent with tilting of the order of only 17–20° away from the ridge axis [*Pariso et al.*, 1991; *Pettigrew et al.*, 1999; *Dick et al.*, 2000; *Allerton and Tivey*, 2001].

[8] While internally consistent, the large-magnitude rotation solutions from the MAR are extremely nonunique, and interpretations based upon these data alone are thus hazardous. Because shifts in the horizontal component of magnetization are unconstrained, from a geometrical standpoint rotation about axes of *any* orientation could have generated

the observed inclination shift. As shown herein, many of the alternative solutions require only minimal rotation magnitudes. Although it is a reasonable first-order assumption that rotations should occur about an axis parallel to the ridge, or perpendicular to corrugations on the OCC surface, because the MAR trends approximately N-S such a rotation axis will be very close in orientation to the GAD direction; hence minor differences in the orientation of the axis chosen will have enormous effects on the resultant magnitude of rotation (see section 5). Moreover, alternative or additional rotations, even of small magnitude, about any other axis will have a far greater effect upon the resultant magnetic inclination direction than will an MAR-parallel one.

[9] Flexural uplift related to adjacent transform boundaries [e.g., *Baines et al.*, 2003], for example, could readily generate rotations, or additional rotations, over and above any associated with the core complex detachment itself. The same is true for any later, postdetachment faulting that is oblique to the spreading axis. Such oblique structures have been documented in the Leg 209 boreholes in the 15°N region (Sites 1268–1274 [*Kelemen et al.*, 2004]), and *Schroeder et al.* [2007] argue that these could potentially be responsible for significant additional rotations over and above any associated with earlier, high-strain fault zones. Likewise at Atlantis Massif spreading direction–parallel faults and oblique faults [e.g., *Blackman et al.*, 2002; *Karson et al.*, 2006] are also identified from the bathymetry. One large spreading direction–parallel north facing scarp at 30°08′N, which separates the morphologically distinct, uplifted and peridotite-bearing Southern Ridge from the gabbro-bearing, deeper Central Dome of the Atlantis Massif [e.g., *Blackman et al.*, 2008; *Canales et al.*, 2008]. This structure has been interpreted as a possible transfer fault with significant normal component [*Karson et al.*, 2006]. Modest rotational strains on any of the above could readily generate the anomalously shallow inclinations observed in the ODP/IODP cores without the need for any rotation to be accommodated on the high-strain detachment fault itself.

[10] There must remain significant doubt, therefore, about the robustness of the inferences from inclination-only paleomagnetic data, that significant tectonic rotations occur in OCC footwalls [*Garcés and Gee*, 2007; *Zhao and Tominaga*, 2009].

2.1.2. Fully Oriented Data

[11] In a recent paper *Morris et al.* [2009] attempted to overcome the limitations of dealing with inclination-only data by reorienting IODP drill cores from Hole U1309D at the Atlantis Massif. Reorientation may be achieved by matching distinct planar features in the cores with their representations on oriented images of the borehole wall acquired using downhole logging tools such as the Formation MicroScanner or Borehole Televiewer, which provide direction data with respect to present-day geomagnetic north [*MacLeod et al.*, 1992, 1994, 1995]. In practice the technique is labor intensive and, because core recovery is rarely complete, unambiguous interpretation is possible only in certain intervals. Nevertheless, *Morris et al.* [2009] successfully determined the horizontal as well as vertical components of remanence directions for intervals of Hole U1309D, documenting that a clockwise vertical axis component of shift of the mean paleomagnetic vector accompanied the shallowing of inclination found previously [*Blackman et al.*, 2006]. These data are consistent with a 46° ± 6° counterclockwise rotation about an assumed horizontal axis of 011° ± 6°, thus parallel to the MAR axis.

2.2. Proposed Methodology

[12] Despite the significant additional constraint brought by the study of azimuthally oriented core, the analysis of *Morris et al.* [2009] still makes an a priori assumption as to the orientation of the rotation axis. Knowledge of the deviation of the paleomagnetic vector away from the reference direction does not in itself allow either the axis or magnitude of rotation to be determined uniquely. Whereas for inclination-only data any rotation axis is geometrically permissible, for fully oriented data the potential axes of rotation are constrained (only) to lie upon a great circle equidistant between the GAD and site vector, with rotation magnitudes varying systematically with position along the great circle (see Section 5). Additional, external, information is necessary to determine which of these possible axes is most appropriate.

[13] We here propose that the most geologically robust method for independently determining both the magnitude and axis of rotation is to utilize the original remanence directions of fully oriented samples in conjunction with local kinematic data measured from shear zones active during (and responsible for accommodating) the rotational strain. With the example presented in this paper we show that rigorous error analysis is essential if the rotation axes and magnitudes are to be properly quantified and uncertainties constrained. Such error

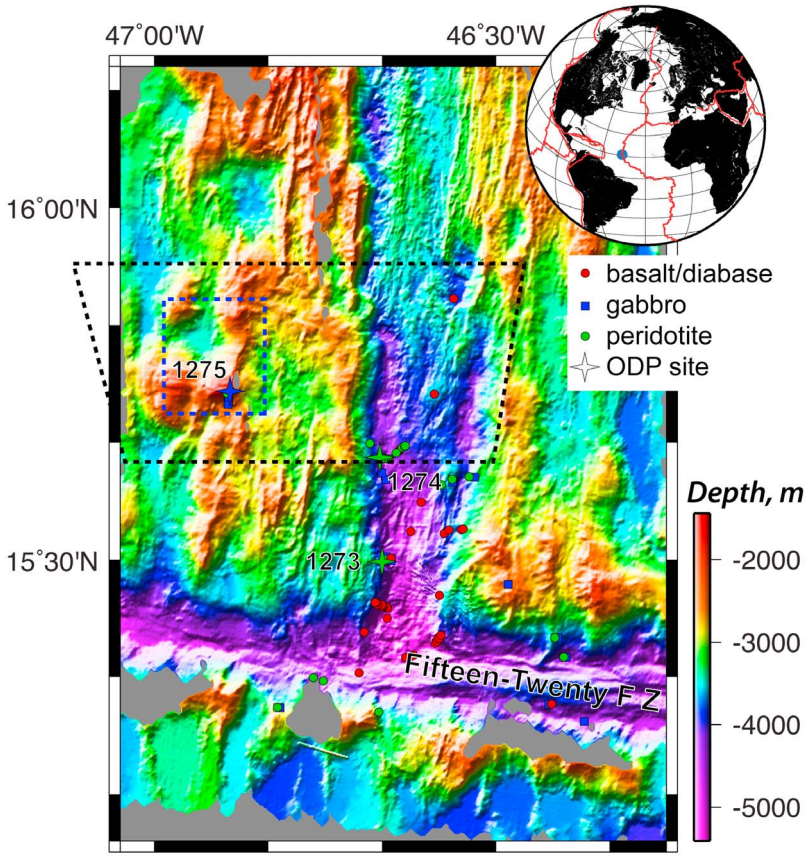

Figure 2. Bathymetry of the Fifteen-Twenty fracture zone area, modified after *Fujiwara et al.* [2003], showing the disposition of lithologies from previous investigations, including three of the ODP Leg 209 sites [*Kelemen et al.*, 2004]. Black dashed box shows the approximate area of view of Figure 3, and blue dashed box shows the area of Figure 4. Inset globe shows the general location of the Fifteen-Twenty region in the central Atlantic Ocean.

analysis is especially important in those regions in which the most geologically likely rotation axes lie close to the local GAD direction (e.g., along any ~N-S trending spreading ridge). The methodology employed herein is optimal not only because it minimizes the a priori external assumptions made in previous studies, but because it can potentially account for and negate the effects of subsequent tectonic complexities.

2.3. The 15°45′N Oceanic Core Complex, Mid-Atlantic Ridge

[14] Geological observations from the axial valley in the vicinity of the Fifteen-Twenty fracture zone on the MAR have revealed that large areas of serpentinized peridotite are exposed on the seafloor over a broad region [e.g., *Cannat and Casey*, 1995; *Cannat et al.*, 1997; *Lagabrielle et al.*, 1998] (Figure 2). Several corrugated OCC massifs occur north and south of the fracture zone, both at the inside and outside corners of the ridge-transform intersections [*Escartín and Cannat*, 1999; *Fujiwara et al.*, 2003].

[15] The 15°45′N OCC is a 250 km^2 broadly flat-topped, corrugated massif lying 35 km north of the Fifteen-Twenty fracture zone and 30 km west of the MAR axis, hence in an outside corner setting (Figure 2). Magnetic anomaly inversions show it to be bracketed by anomalies C2n and C2An, on the basis of which it is considered to have been formed and active within the interval ~2.5 to 2.1 Myr. ago, assuming a half spreading rate of 13.0 km/Myr on the western flank of the axis [*Fujiwara et al.*, 2003]. The OCC's upper surface is prominently corrugated, characterized by spreading direction–parallel striations and corrugations at wavelengths from cm up to 10 km and amplitudes of up to a kilometer [*MacLeod et al.*, 2002]. These show a mean trend of 272.1° ± 3.5°, perpendicular to the strike of the ridge axis, and very similar to the AF-NA spreading

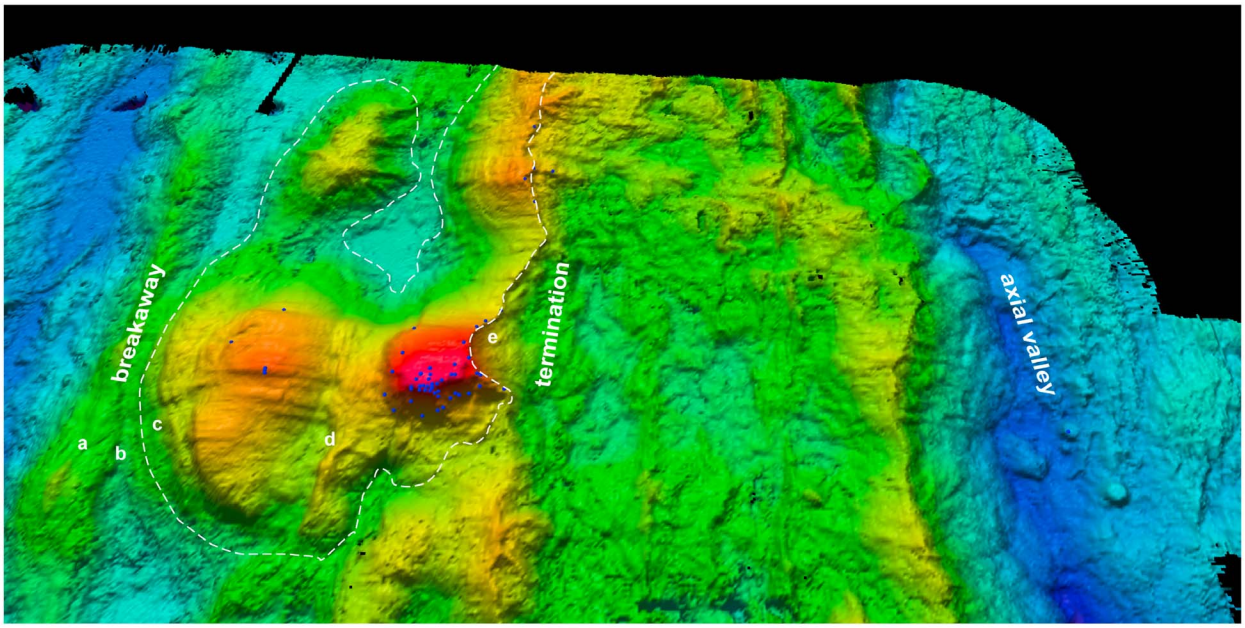

Figure 3. Oblique 3-D view of bathymetry of 15°45′N OCC, showing principal physiographic features. No vertical exaggeration. The oldest part of the OCC, the breakaway, lies at left, approximately 45 km west of the center of the axial valley; individual features a to c within the breakaway region are described in the text. The corrugated surface of the OCC, indicated approximately by a white dashed line, is bisected by an outward dipping fault zone at point d. Approximately 27 km from the center of the axial valley the OCC is terminated by a continuous ridge-dipping normal fault that, at point e, is heavily modified by mass wasting. Blue dots indicate locations of BRIDGE drill sites detailed in Figure 4. Color palette is similar to that of Figure 4, with deeper areas in blue and shallower areas in orange/red.

direction of 276° (NUVEL-1/1A [*DeMets et al.*, 1990, 1994] and REVEL [*Sella et al.*, 2002]).

[16] The outer (distal) extremity of the OCC, the breakaway, lies approximately 43 km west of the axis of the median valley. It is marked by a smooth slope dipping away from the ridge axis at ~15–30° west (Figure 3a). On the basis of TOBI side scan sonar imagery [*MacLeod et al.*, 2002] this slope is thought likely to be heavily sediment-covered volcanic terrain. It is separated from the elevated, corrugated massif by a laterally persistent, ridge-parallel, inward dipping fault scarp up to 400 m high that dips 20–30° east (Figure 3b), and thence by a series of small, steeper outward dipping faults (40–45° west) that are collectively responsible for more than 1 km of relative elevation of the corrugated detachment fault surface to their east (Figure 3c). Another zone of outward dipping faults trending N-S in the center of the OCC (at ~46°55.4′W) divides the corrugated surface in two halves (Figure 3d). These structures, in combination with the large amplitude undulations of the detachment surface, result in the core complex being disposed on the seafloor as four distinct, relatively elevated corrugated knolls (Figure 3). The SE knoll is the shallowest, at ~1450 m water depth, and has a planar, prominently corrugated surface that dips at up to 5° west. The SW knoll, at 1880 m water depth, displays a gentle convex-upward curvature about an axis parallel to the ridge axis, dipping up to 17° east on its eastern (ridgeward) side and 11° west on its western side. The OCC as a whole is terminated on its eastern side at 46°52′ to 46°53′W, approximately 26 km west of the center of the axial valley, by a steep (up to 55°) E dipping fault scarp with a maximum of 1400 m of vertical throw, now heavily modified by mass wasting [*Escartín et al.*, 2003] (Figure 3e). This structure appears to have been the one primarily responsible for accommodating the uplift, and probable minor back tilting, of the OCC as the principal detachment fault was terminated. Detachment faults terminated and dissected by later high-angle normal faults such as this have been documented elsewhere, and are interpreted to be a consequence of a rapid increase in flexural rigidity and hence strengthening of the OCC footwall as it moves away from the spreading axis [*Cannat et al.*, 2009].

[17] Sampling of the surface and flanks of the 15°45′N massif reveal the surface of the massif to

be an exposed low-angle fault zone characterized by talc-chlorite-tremolite schists [*MacLeod et al.*, 2002; *Escartín et al.*, 2003]. These fault rocks are described further in section 4.1 below. The footwall of the OCC, exposed on the flanks of the 15°45′N massif, is dominated by partially serpentinized harzburgites, dunites and troctolites. These are mantle-derived rocks, and display characteristic mesh-textured serpentinization textures [see *MacLeod et al.*, 2002, Figure 3c; *Escartín et al.*, 2003, Figure 4] indicating that they have suffered little or no pervasive post-serpentinization deformation. Macroscopic evidence for high-strain, high-temperature, ductile pre-serpentinization deformation was found in only one sample, representing <0.5% of the (550 kg of) serpentinized peridotite samples dredged or drilled from the vicinity of the 15°45′N OCC during cruise JR63. This suggests that early high-temperature deformation in the lower lithosphere was very localized.

[18] Whereas serpentinized peridotites predominate across most of the area of the footwall of the 15°45′N OCC, gabbro is present at its southeastern corner, immediately west of the termination [*Matsumoto et al.*, 1998; *Fujiwara et al.*, 2003]. Our detailed exploration and sampling of this area reveals that the gabbro forms a discrete body, surrounded by peridotite, that extends ≥10 km in the ridge-parallel direction (N-S), ≥5 km along the flow line (E-W), and >1 km vertically, that was intruded to within no more than a few tens of meters of the detachment fault [*MacLeod et al.*, 2002; *Escartín et al.*, 2003] (Figure 4). This gabbro was sampled during ODP Leg 209 at Site 1275 [*Kelemen et al.*, 2004]. Complex intrusive relationships in the ODP cores are interpreted as supporting a model in which the gabbro body was formed by a protracted episode of intrusion, similar to that inferred for the Atlantis Massif, rather than as a single pluton [*Kelemen et al.*, 2004; *Blackman et al.*, 2006; *Grimes et al.*, 2008].

[19] The JR63 drilling also revealed the presence of abundant diabase bodies in the vicinity of the gabbro in the southeastern part of the 15°45′N OCC. Diabase forms 48% of recovered igneous material in cores here as opposed to 13% elsewhere. It intrudes serpentinized peridotite and, more rarely, gabbro in the OCC footwall. Noting the spatial association with the gabbro body, *MacLeod et al.* [2002] suggested that the diabase intrusions emanated from it, albeit probably fed from deeper than the exposed level. Diabase also intrudes the detachment fault zone itself, as described in section 4. Chilled margins to the diabase bodies (including some multiple, diabase–diabase contacts) have low-angle present-day dips [see *Escartín et al.*, 2003, Figure 4]. A similar relationship is observed in cores from Site U1309 at the Atlantis Massif and is interpreted as evidence for sill complexes there [*Blackman et al.*, 2006]. The original geometry and origin of the 15°45′N diabase intrusions are considered further in section 6.2.

3. Oriented Core Sampling Using the "BRIDGE" Seabed Rock Drill

[20] The samples that form the subject of this paper were collected during RRS *James Clark Ross* cruise JR63 using an electrically operated robotic seabed rock coring device designed, built and operated by the British Geological Survey. The "BRIDGE" seabed drill, illustrated by C. J. MacLeod (frontispiece, *Geology*, *30*(11), 2002), is so named because the original development of the drill was funded by the NERC British Ridge Inter-Disciplinary Global Experiment program. It has the ability to collect meter-long, 35 mm diameter, oriented rock cores from hard substrates in water depths of up to 5000 m from a conventional research ship. The device utilizes a high-speed rotary diamond drill mounted vertically on a stainless steel tripod frame [*Allerton et al.*, 1999]. It has the unique ability (for a seabed device) of being able to take geographically oriented cores directly. A (nonmagnetic) tungsten carbide scriber is fitted immediately above the core catcher on the inside of a nonrotating inner core barrel, and carves a scratch along the length of the core as it enters the barrel. The scriber is fixed relative to the drill frame, whose orientation is measured by means of two fluxgate compasses mounted in different positions on the frame (one approximately a meter above the other). The compasses are calibrated by spinning the drill in the water column upon descent. The full geographical orientation of the cores can be recovered by combining the compass measurements with readings from the accompanying pitch and roll sensors. The potential for biasing effects as a result of the influence of highly magnetic rocks at the seafloor may be monitored by looking for deviations between the two compass measurements as the seafloor was approached. To date no significant effect has ever been noticed, even at the most oxide-rich gabbro or heavily serpentinized peridotite drill sites.

[21] On cruise JR63 the BRIDGE drill was deployed via an armored coaxial power and hoist cable, also

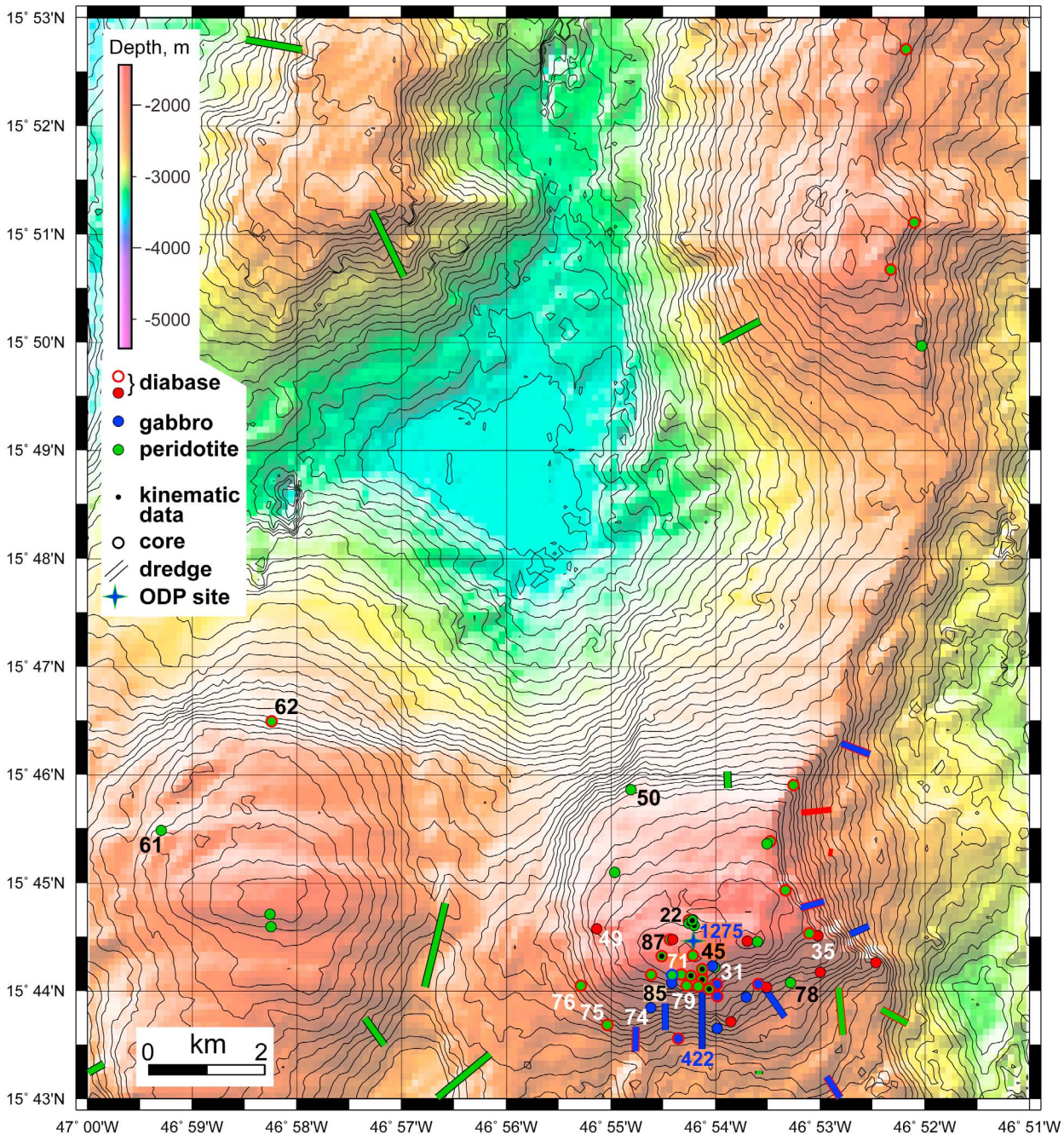

Figure 4. Shaded relief bathymetry map of the southern part of the 15°45′N OCC showing summary of sampling results. Locations of JR63 dredge and BRIDGE drill sites are shown by thick lines and circles, respectively; ODP Site 1275 is indicated by a star, and *Shinkai* dive 422 track is labeled as a thick line. Numbers refer to BRIDGE drill sites (prefixed by "BR") analyzed here for paleomagnetism: bold black numbers refer to sites used in derivation of mean magnetization direction, and white numbers refer to those not used, for reasons discussed in text. Small black circles denote sites from which kinematic measurements were made, as presented in Figure 6.

used for communications and for relaying photos from a camera mounted on the drill frame up to the surface to aid site selection (a fiber-optic cable may instead be used). The drill successfully recovered samples in water depths of up to 4500 m and from seafloor with slopes of up to 44°. Cores were recovered from 63 sites (49 reliably oriented) from 72 BRIDGE drill deployments in 12 days of operations. At several sites we photographed a hard seafloor pavement displaying striations parallel to the

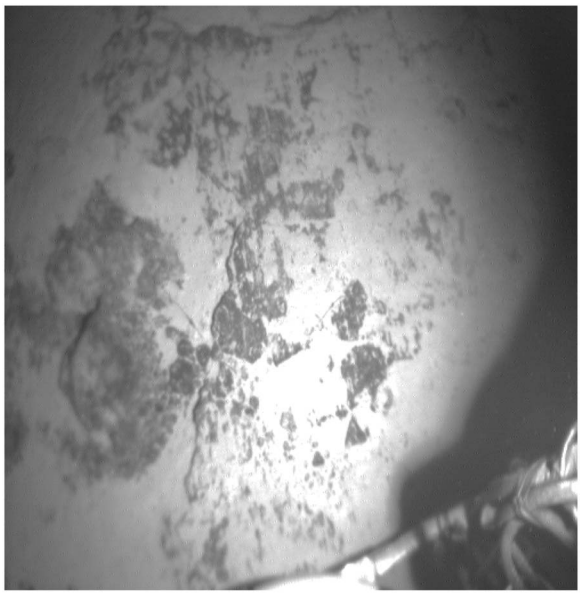

Figure 5. BRIDGE drill seabed photograph, Site BR22. Field of view is approximately 4 m, looking toward 104°. Leg of drill rig is at bottom right. Note striations trending WNW-ESE.

larger-scale corrugations and spreading direction (Figure 5).

4. Results

4.1. Structure and Kinematics of Detachment Fault Rocks

[22] High-strain fault rocks were recovered in almost all BRIDGE drill core sites located on the corrugated surface of the 15°45′N OCC. Undeformed greenschist facies diabase samples (with chilled margins) recovered at some of the sites are interpreted to be (locally) postkinematic intrusions into the fault zone; however, the presence of diabase porphyroclasts within some fault rocks demonstrates that diabase intrusion bracketed the period of deformation [*MacLeod et al.*, 2002]. The thickness of the damage zone associated with the detachment fault is not known precisely but is constrained from the JR63 sampling to be ≤50 m thick [*Escartín et al.*, 2003], and from the ODP drilling to be potentially 30–50 m or less [*Kelemen et al.*, 2004]. The presence of essentially undeformed gabbros and mesh-textured, passively serpentinized peridotites in the immediately subjacent footwall attests to the efficiency of localization of deformation onto the detachment fault.

[23] The fault rocks recovered from the surface of the OCC are assumed to be responsible for its exhumation. They are dominated by intensely foliated talc–tremolite ± chlorite schists and a lesser proportion of cohesive foliated cataclasites [*MacLeod et al.*, 2002], described in detail by *Escartín et al.* [2003]. In summary, the fault schists possess greenschist facies assemblages, with complex microstructures indicative of extremely high strains, and evidence for both ductile and brittle deformation. The former is revealed by syntectonic recrystallization and growth of talc, chlorite and amphibole within the foliation; the latter by porphyroclasts of amphibole and reworked amphibole schist surrounded by the foliated matrix, and by foliated amphibole ± chlorite cataclasites [*Escartín et al.*, 2003]. Serpentine is rare, and where present is overprinted by talc [*Kelemen et al.*, 2004].

[24] No evidence has been found for any higher-temperature precursory deformation in the fault rocks from the corrugated detachment fault surface at 15°45′N or in the adjacent footwall; crystal-plastic deformation in the footwall gabbros [*Escartín et al.*, 2003; *Schroeder et al.*, 2007] is rare, very weak and is not spatially associated with the detachment surface, suggesting that the gabbro pluton cooled rapidly through the temperature interval of ductile deformation (>~650°C). Evidence from Site 1275 suggests that fluid ingress into the gabbro was facilitated by brittle deformation and cracking at temperatures in excess of 500°C, potentially as high as 770°C [*Kelemen et al.*, 2004].

[25] The talc–tremolite ± chlorite schists are derived from a predominantly ultramafic protolith, as shown by the presence of relict chromite grains, though with evidence for some essential mafic component [*Escartín et al.*, 2003]. The contribution of silica from the latter allows formation of talc rather than serpentine [e.g., *Boschi et al.*, 2006], serpentine being very rare in the fault rocks. Deformation was accompanied by extensive chemical exchange with black smoker–type fluids at greenschist facies temperatures (~350°C) prior to the intrusion of the diabase bodies [*McCaig et al.*, 2007, 2010]. Absence of the talc–tremolite–chlorite assemblages from the adjacent undeformed footwall rocks (gabbros and serpentinized peridotites) demonstrates that the high-flux fluid flow was channeled efficiently along the fault zone. Strain localization was clearly aided by high fluid pressures and reaction softening caused by formation of the extremely weak hydrous secondary minerals along the fault zone. Talc in particular is especially weak, experiments demonstrating coefficients of friction as low as ~0.05 to 0.23 over a broad range of temperatures

and pressures [*Escartín et al.*, 2008a; *Moore and Lockner*, 2008, 2011].

[26] The fault rocks from the surface of the 15°45′N OCC display *l*-*s* tectonite fabrics resulting from noncoaxial deformation within the detachment shear zone. Foliations are well developed, defined primarily by the strong preferred orientation of fine-grained talc, amphibole and chlorite aggregates. Fabrics are complex, often displaying microfolded and anastomosing foliations cut by shear band cleavage, and S-C structures [*MacLeod et al.*, 2002, Figures 3a and 3b; *Escartín et al.*, 2003, Figure 4]. Lineations, defined either by mineral growth or by striations and polishing, are visible on many foliation surfaces.

[27] The fault rocks are generally cohesive, though very fragile, the talc-bearing schists in particular being easily parted along the foliation planes. Although schistose fault rock was observed in 28 of the BRIDGE drill cores, in almost half of the cores the recovered material was highly fragmented and no fiducial reference orientation was preserved. With reference to the BRIDGE drill seabed photographs it is evident that some of the disaggregation of the talc schists resulted from seafloor weathering of the fault surface. In other cases, however, including some in which a flat, striated rock pavement was visible on the seafloor (e.g., Figure 5), the fault rock at the seabed was clearly so weak that it was ripped apart into thin biscuits bounded by the schistose foliation planes by the torsion imparted during the high-speed diamond drilling operations. From these observations it may be readily understood why ODP-type drilling, using low-speed tricone bits from a surface drillship, has been largely unsuccessful in recovering this fragile fault rock from OCC surfaces in operations to date.

[28] In 11 BRIDGE drill cores from the surface of the 15°45′N OCC it was possible to recover the orientations of the foliations and, in many cases, lineations in the schistose fault rocks (48 and 29 measurements, respectively). In the first instance measurements were made relative to the core scriber mark using a specially made goniometer; these data were later rotated to geographical coordinates by correcting for the pitch, roll and heading of the drill.

[29] The true orientations of foliations and associated lineations are shown in Figure 6a. The measured foliation planes are restored to a shallow dip angle, 70% of planes dipping at less than 30°. The poles to these planes display a weak girdle distribution dispersed about an approximately ridge-parallel axis; that is, foliation planes show a moderate spread of dips, both toward and away from the present-day spreading axis, but with generally ridge-parallel strikes. The maximum density of poles corresponds to a plane striking 199° and dipping 5° west. The spread of orientations of the foliation planes (Figure 6a) is similar to, though slightly more dispersed than, the distribution of slopes of the OCC surface itself (area of corrugated seafloor), which has an almost identical mean orientation of 209° strike and dip 2° west (Figure 6b). The variability in slope of the exposed fault surface reflects both its curved form in a ridge-parallel direction and the spreading direction–parallel curvature associated with the corrugations themselves. Though parallel to the fault surface overall, the small-scale variability of orientations (primarily of dip) measured in the schistose foliations is attributed primarily to the complex, commonly sigmoidal, fine-scale S-C type internal fabrics displayed by many of the fault rocks. These fabrics are comparable to those described by *Karson et al.* [2006] from the Lost City area of the Atlantis Massif.

[30] Lineations in the fault rocks display a well-defined mean vector *L* of 273.2°; 7.5° and α_{95} of 9.0° (k = 10; Figure 6a). The azimuth of this vector is identical within error to the arithmetic mean trend of the corrugations on the fault surface (272.1° ± 3.5°; Figure 6c), and the computed spreading direction (276° [*Sella et al.*, 2002]), a convincing demonstration of the BRIDGE drill's core orientation capability. In some instances a clockwise sense of rotation and asymmetry between the foliation ("S") and shear bands ("C") could be observed in sections cut parallel to the lineation, demonstrating a bottom-to-the-west shear sense [*Berthé et al.*, 1979].

4.2. Paleomagnetism

4.2.1. Analytical Methods

[31] Whereas material was recovered from 63 of the 72 sites occupied during BRIDGE drill operations during cruise JR63, only a minority of the cores were suitable for paleomagnetic investigation. Reasons for this included unsuitable lithology (e.g., fault rocks); severe fragmentation of the core; lack of preservation of a scribed orientation mark; and suspicion (from seabed photo, or nature of the recovered lithologies) that the core did not sample outcrop. It was nevertheless rarely possible to determine with certainty that the site was fully in situ bedrock, because of the limited field of view of the BRIDGE drill camera and near-ubiquitous presence

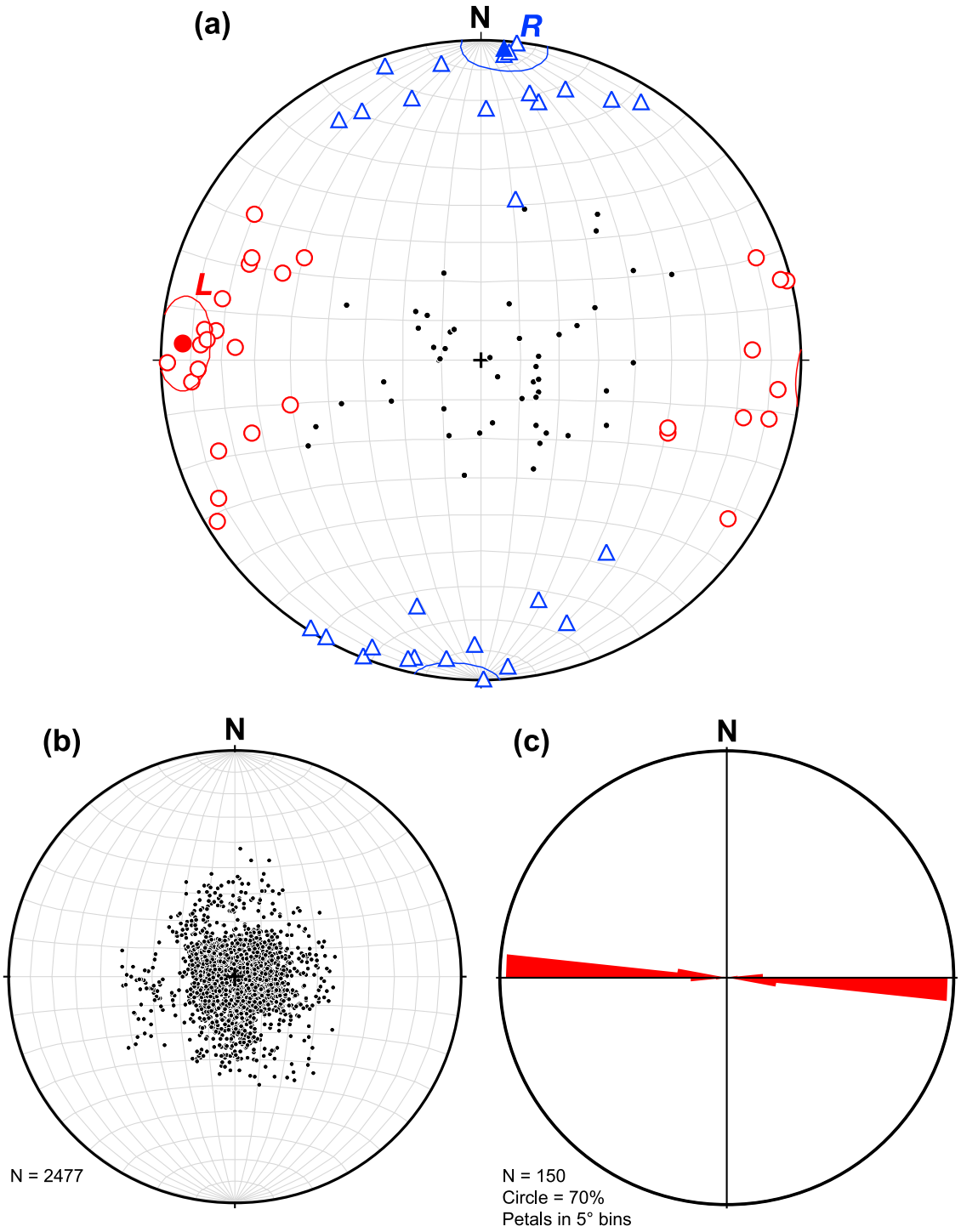

Figure 6. (a) Reoriented kinematic data from JR63 cores from the 15°45′N OCC. Equal angle lower hemisphere projection of orientation of foliations (poles to planes; black) and lineations (red) of high-strain schistose fault rocks from 11 sites on the 15°45′N detachment fault surface. Blue triangles are no-slip vectors: the perpendicular to the slip direction on a given shear plane, inferred to represent the axis of rotation effected by that structure. *L* and *R* represent the mean lineation and no-slip vectors, respectively. (b) Poles to planes of slopes on corrugated surface of 15°45′N OCC, derived from gridded multibeam bathymetry data. $N = 2477$. Data correspond to a mean plane of 009°/2°E. (c) Rose diagram of combined azimuths of corrugations, measured from multibeam bathymetry, and striations, measured from TOBI side scan sonar images, from 15°45′N OCC surface. Mean trend = 272.1° ± 3.5° angular deviation, $N = 150$, and plot data are binned at 5° intervals.

of pelagic sediment and/or talus surrounding each outcrop (e.g., Figure 5).

[32] The results of paleomagnetic investigations attempted on apparently suitable, undeformed core material from 16 sites are presented here. All localities are either from the flanks of the OCC or from the corrugated surface itself (Figure 4) and assumed to be windows through the fault zone. The sites are all interpreted as belonging to the footwall of the detachment fault zone. The subset of the sites used in the later analysis (see sections 4.2.3 and 5) are estimated all to have been originally no more than 50 m stratigraphically away from the fault zone.

[33] The 35 mm diameter oriented cores from the BRIDGE seabed rock drill were subsampled perpendicular to the axis of the cores using a bench-mounted drill, thereby obtaining 11 mm diameter, 35 mm long minicores. Wherever possible duplicate sampling was performed on the same BRIDGE core to obtain a second and sometimes a third minicore in order to test for reproducibility. Each minicore was then divided into 3 samples named a, b and c.

[34] All samples were first measured for their natural remanent magnetization (NRM). Samples with magnetizations in excess of 10^{-3} A m^{-1}, corresponding to a bulk measurement of the order of 10^{-9} A m^2, were selected for demagnetization. Whenever possible one subsample was selected for alternating field (AF) demagnetization while another from the same minicore was selected for thermal demagnetization. Thermal demagnetization experiments were performed at the Institute de Physique du Globe de Paris (IPGP), and AF demagnetization at Ecole Normale Supérieure (ENS), Paris; in each laboratory measurements were performed using a 2G cryogenic magnetometer. Line-fitting techniques [*Kirschvink*, 1980] were used to determine the direction of magnetization. In a few cases (see Table 1) the great circle analysis technique was used instead. *Fisher* [1953] statistics (or mixed statistics when great circles were necessary) were performed on units with multiple successfully demagnetized samples. All graphical treatments were done using the Paleomac package [*Cogné*, 2003].

[35] After AF demagnetization some of the samples were selected to make polished thin sections for observations using an S-2500 Hitachi scanning electron microscope (SEM) in backscattered mode at the Laboratoire de Géologie, ENS. Energy-Dispersive X-ray Spectroscopy (EDS-X) was used during SEM observations to obtain semiquantitative chemical analyses. The accuracy of our semiquantitative analyses on iron and titanium phases was monitored by analyzing two standards during each SEM session. From this we estimate the accuracy to be better than 5%.

[36] Approximately 300 mg of powdered fragments from the AF demagnetized samples were also used for thermomagnetic measurements carried out in heating/cooling cycles from 20°C up to 700°C (or 620°C in a few cases) in an argon atmosphere using an AGICO KLY3 susceptibility meter with a CS3 furnace. Hysteresis loop measurements at ambient temperature and a maximum field of 600 mT were made on sample fragments using a translation magnetometer at the IPGP St Maur laboratory.

4.2.2. Alternating Field and Thermal Demagnetization

[37] The NRM intensities of samples selected for AF and thermal treatment encompass almost four orders of magnitude, from the threshold of 10^{-3} A m^{-1} for some of the diabase samples up to 7.5 A m^{-1} for one dunite (BR78). Variability in NRM intensity in samples from the same BRIDGE drill core is always low; mean values are accordingly reported in Table 1.

[38] The BRIDGE drill employs high-speed diamond drilling (typically ~250 rpm) and, in consequence, samples do not display the typical drill string–induced magnetic overprint that so plagues ODP/IODP core material. Following standard AF and thermal treatment we were accordingly able to isolate a primary component of magnetization in 16 out of the 19 BRIDGE cores selected (Table 1).

[39] During thermal treatment the progressive demagnetization of the samples from 20°C up to 540°C or 580°C suggests that magnetite is a significant carrier of the NRM. Examples of typical demagnetization diagrams are shown in Figures 7a–7d using the *Zijderveld* [1967] projection. Duplicate samples from the same BRIDGE drill core always show similar directions, as seen in the examples in Figures 7a–7d. In a few cases complicated demagnetization behavior or pronounced secondary components were observed (see Figures 7e and 7f), associated with (1) samples with low magnetization (some of the diabases) and (2) gabbros, which gave systematically lower quality results. In these cases principal components could sometimes not be determined, presumably due to complex magnetization linked to low magnetic stability. In four cases (sites BR31, BR35, BR76 and BR79) the site direction is determined from only one sample,

Table 1. Paleomagnetic Results[a]

Site (Pc)	Lithology	Latitude (°N)	Longitude (°W)	Water Depth (m)	Minisample/ Treatment	n/N	Mean NRM (A m^{-1})	Thermomagnetic Group	Dec (deg)	Inc (deg)	α_{95}	Comments[b]	Utilized for Mean Direction?
BR22 (1)	Harzburgite	15°44.6355′	46°54.2468′	1614	3/AF, 2/Th	4/5	5.5×10^{-1}	I	202.8	−6.8	9.2		Y
BR31 (1)	Diabase	15°44.1464′	46°54.1328′	1610	2/AF	1/2	1.2×10^{-3}	II	150.2	−10.4	NA	weak	N
BR33 (3)	Diabase	15°44.2058′	46°54.1351′	1581	2/AF	0/2	1.1×10^{-3}	–	–	–	–	weak	N
BR35 (1)	Diabase	15°44.5130′	46°53.0301′	1813	1/AF, 1/Th	1/2	4.1×10^{-1}	II	260.9	−15.6	NA		N
BR45 (7)	Diabase	15°44.3295′	46°54.2240′	1544	2/AF, 1/Th	3/3	3.7×10^{-1}	I	023.9	20.0	5.9		Y
BR49 (1)	Diabase	15°44.5784′	46°55.1447′	1750	2/AF, 2/Th	4/4	1.2	III	151.8	−19.1	3.7		N
BR50 (2)	Dunite	15°45.8670′	46°54.8162′	2044	2/AF, 1/Th	3/3	6.3	I	178.5	−13.7	6.7		Y
BR61 (3)	Harzburgite	15°45.4899′	46°59.3037′	2091	1/AF, 1/Th	2/2	2.2	I	170.9	−5.0	7.2		Y
BR62 (19)	Harzburgite	15°46.4985′	46°58.2508′	2305	2/AF, 1/Th	2/3	1.1	I	028.3	10.3	7.1	1 GtC	Y
BR71 (9)	Diabase	15°44.1435′	46°54.2418′	1586	1/AF, 1/Th	2/2	1.5×10^{-2}	II	338.1	−21.7	2.7	1 GtC	N
BR73 (1)	Gabbro	15°43.5619′	46°54.3663′	2295	3/AF, 1/Th	0/4	3.3×10^{-2}	–	–	–	–		N
BR74 (1)	Gabbro	15°43.8461′	46°54.6285′	1934	5/AF, 3/Th	7/8	1.8×10^{-2}	II	253.4	71.5	12.8	significant dispersion	N
BR75 (1)	Diabase	15°43.6818′	46°55.0414′	2186	4/AF, 2/Th	6/6	2.1×10^{-2}	III	282.5	35.7	3.7		N
BR76 (1)	Diabase	15°44.0500′	46°55.2935′	2066	2/AF	1/2	1.1×10^{-1}	II	104.9	66.7	NA		N
BR78 (2)	Dunite	15°44.0865′	46°53.2914′	2080	3/AF, 2/Th	5/5	6.6	I	196.8	−18.8	8.9		Y
BR79 (3)	Diabase	15°44.0482′	46°54.1721′	1656	2/AF	1/2	3.4×10^{-3}	II	277.8	−23.2	NA	weak	N
BR85 (1)	Gabbro	15°44.0761′	46°54.4287′	1674	4/AF, 1/Th	5/5	6.1×10^{-1}	I	208.5	−20.3	16.7	1 GtC, significant dispersion	Y
BR87 (2)	Diabase	15°44.4795′	46°54.4253′	1563	3/AF, 1/Th	4/4	4.2×10^{-3}	II	205.7	−13.2	18.6	1 GtC, weak	Y
BR90 (7)	Diabase	15°44.0179′	46°54.0682′	1745	3/AF	0/3	1.5×10^{-3}	–	–	–	–	weak	N

[a]Minisample/treatment, number of minisamples demagnetized with respect to the type of demagnetization; Pc, piece number; AF, alternating field demagnetization; Th, thermal demagnetization; n/N, number of samples included/measured; Dec, declination; Inc, inclination; α_{95}, precision parameter.

[b]Note that 1 "GtC" means that one great circle was used in the analysis instead of Kirschvink principal component analysis, and "weak" means that the NRM was only of the order of 100 times the noise level of the magnetometer (10–11 A m^2).

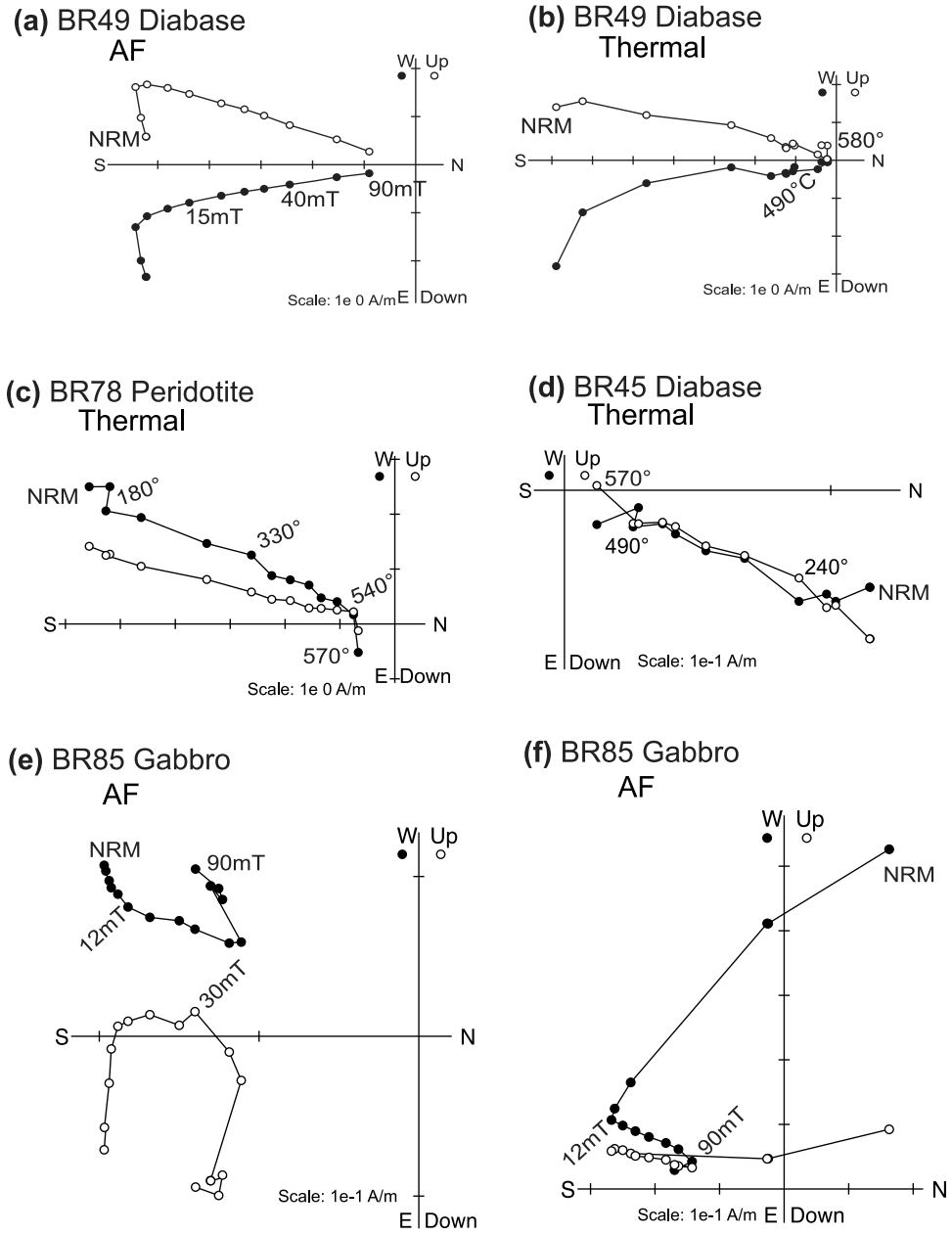

Figure 7. (a–f) Zijderveld plots illustrating typical demagnetization characteristics of JR63 cores.

and these data should be taken with much caution. We did not observe the complex multicomponent behavior that has been encountered in some MAR gabbro cores [e.g., *Morris et al.*, 2009].

4.2.3. Mean Paleomagnetic Direction

[40] Eight of the sites plotted in Figure 4 possess consistent, well-clustered mean directions. Six are associated with reversed polarity and SSW declination (BR22, BR50, BR61, BR78, BR85, BR87), consistent with the negative inclinations determined in cores from ODP Site 1275 [*Kelemen et al.*, 2004], which was sited in the same, SE part of the 15°45′N OCC as the majority of the BRIDGE drill cores (Figure 4). All these samples are inferred to belong to the C2r anomaly identified in the magnetic mapping of the Fifteen-Twenty fracture zone region of *Fujiwara et al.* [2003]. Two samples are associated with an antipodal normal polarity and NNE declinations (BR45, BR62). BR45 is a diabase from the SE portion of the OCC and therefore probably corresponds to a later intrusion event (C2n or younger, i.e., ≤1.95 Ma). Sample BR62 is located on

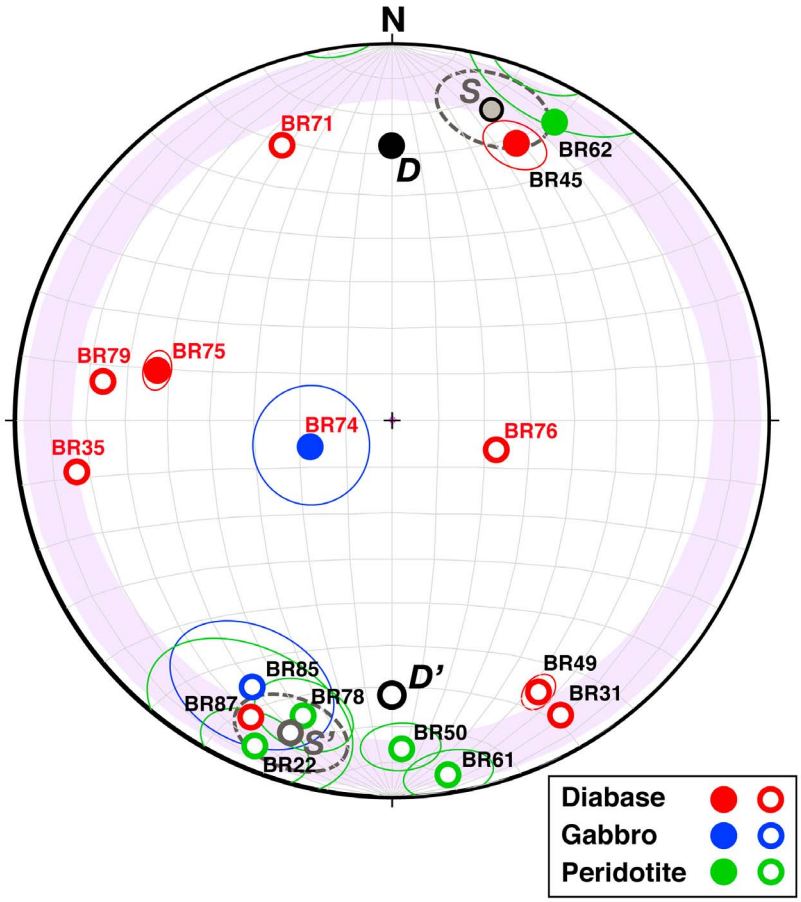

Figure 8. Summary of stable magnetic remanence directions and confidence cones for individual drill sites. Open symbols are in the upper hemisphere. *D* and *D′* are the reference geocentric axial dipole direction (normal and reversed polarity, respectively), and *S* and *S′* are the mean vectors of assumed in situ drill sites (labeled in black) used in the subsequent analysis. Original data and demagnetization characteristics are given in Table 1. Lilac band delineates the range (angular deviation) of inclinations in gabbros from ODP Site 1275.

the SW part of the 15°45′N OCC at the edge of positive magnetic anomaly C2An [*Fujiwara et al.*, 2003], and is inferred to have acquired its magnetization at ≥2.58 Ma. Of the remaining sites, all but one of diabase, two (BR31 and BR49) show (negative) inclinations that are similar to the well-clustered sites but with pronounced SSE declinations setting them away from the SSW directed group. The remaining six (BR35, BR71, BR74, BR75, BR76, BR79) show scattered, random directions. There are several reasons why these directions are unlikely to be of geological significance. Because the BRIDGE drill only penetrates ≤1 m subsurface there is always the potential that the cores will have been affected by surficial processes, particularly on steep slopes. All the "anomalous" sites are located on the steep (up to 35°) slopes of the southern flank of the OCC massif; furthermore, this area is very close to the termination of the OCC, which *Escartín et al.* [2003] suggest on morphological grounds to have been affected by extensive land slipping. On balance we suggest it most likely that we did not sample in situ outcrop at these sites, and we therefore exclude them from our analysis.

[41] Projecting all remaining directions as if of normal polarity, the eight sites show a mean trend with declination of 017° and inclination of 14° (hereinafter written 017°; 14°) and α_{95} cone of confidence of 10° and k = 29 (Figure 8). The mean direction calculated on a sample-by-sample basis ($N = 27$) is similar (018°; 14°, $\alpha_{95} = 5°$ and k = 29). Scatter in paleomagnetic directions is commonly evaluated by the angular standard deviation (ASD) of the corresponding virtual geomagnetic poles, allowing us to estimate how well the paleomagnetic secular variation is sampled by a given directional set and therefore whether the mean direction

obtained is likely to be representative. We thus transformed our individual directions to virtual paleomagnetic poles and calculated the ASD. The value obtained for the eight selected sites is 14.1°, a figure that is in full agreement with the value expected for a site latitude of 15°N (= 13–14°, using the model of, e.g., *Quidelleur and Courtillot* [1996]). If BR49 and BR31 are included the ASD increases drastically to 22.6°, corresponding to a value well above the reference curve for the location. This strengthens confidence in our selection of the subset of the eight most consistent sites in calculating a mean direction.

[42] Hereinafter we therefore take a vector, *S*, of 017°; +14° (and α_{95} = 10°) as representative of the mean primary remanence direction of the in situ sample sites from the footwall of the 15°45′N OCC (Figure 8). This direction can be contrasted with the expected GAD direction *D* for the area of 000°; 28°. The difference between *D* and *S* is greater than the 10° uncertainty in *S* and we here make the assumption that it results from a tectonic rotation of the footwall subsequent to acquisition of the magnetization. The shallower than expected (reversed) inclination was also encountered in ODP Site 1275 cores: in Hole 1275B the mean inclination was −9.1°, and in Hole 1275D it was −6.5° in the upper and −13.4° in the lower part of the hole [*Garcés and Gee*, 2007].

4.2.4. Magnetic Mineral Identification From Scanning Electron Microscopy

[43] The variable nature of the rocks used for paleomagnetic experiments (gabbro, diabase, peridotite) and their alteration history, from serpentinization reactions to low temperature alteration, led us to examine the magnetic mineralogy with care. Identification of magnetic minerals was first performed using SEM observations in association with EDS-X analysis. Representative samples were selected and detailed analyses were made on peridotite (BR22, BR61, BR50, BR78), gabbro (BR74, BR85) and diabase thin sections (BR75 and BR49). Examples of SEM images are shown in Figure 9. The proportions of magnetic phases in the observed thin sections vary greatly from sample to sample. Possible contributors to the magnetic behavior of our samples detected using EDS-X analysis are given below, listed by importance of occurrence in the samples: (1) Iron oxide interpreted as being magnetite (Fe_3O_4) was detected in all samples at various concentrations and size: it was very abundant in all peridotites and disposed along serpentine veins (see Figure 9c); it was localized and not very abundant in gabbros (see Figures 9a and 9c); and it was detected rarely, and as tiny grains, in diabase samples. (2) Chrome spinel solid solution series minerals ($Fe_{1+x}Cr_{2-x}O_4$, with $0 < x < 2$) containing minor amounts of Mg and Al were detected in peridotites BR61, BR78, BR50 and BR22 (see Figure 9b) and additionally, with minor amounts of Ti, were detected in gabbro BR74 (Figure 9a). (3) Fe sulfides with compositions consistent with pyrite (FeS_2), pyrrhotite (Fe_7S_8 and/or Fe_8S_9) and chalcopyrite ($CuFeS_2$) were observed in all lithologies: gabbros BR85 and BR74 (see Figure 9a), diabase BR49, and serpentinized peridotites BR22 and BR50. (4) Ti-bearing phases, in particular titanomagnetite with dendritic shapes ($Fe_{3-x}Ti_xO_4$, with $0 < x < 1$), are abundant in diabase sample BR49 (see Figure 9d); ilmenite was very common in diabase BR75; and titanite was present in BR75 and also gabbros BR74 and BR85.

4.2.5. Curie Temperature Measurements

[44] Following the thermomagnetic experiments samples can be divided into three different groups. Samples from the first group (Group I) are the most common, and display behavior similar to that shown in Figure 10a. All peridotite samples (BR22, BR50, BR61, BR62 and BR78) with the addition of diabase sample BR45 and gabbro sample BR85 belong to this group. Samples have mass-normalized susceptibility of the order of 1×10^{-5} m^3 kg^{-1} (for peridotites) and 3×10^{-6} m^3 kg^{-1} to 1×10^{-6} m^3 kg^{-1} for the gabbro and diabase samples, respectively. All show an increase in susceptibility upon heating >120°C; beyond 290°–320°C a decrease takes place. In some cases another moderate increase in the 440–500°C range is noticeable. The samples lose all their magnetic susceptibility around 580°C–590°C. Upon cooling the phases with the highest Curie point are the only ones remaining. The increase in susceptibility between 120°C and 340°C on the heating curve and its subsequent absence on cooling reflects the transformation of a magnetic phase during heating. The nature of this low-temperature phase cannot be determined from thermomagnetic curves alone. The small increase observed around 440°C–500°C in a few samples is similar to that observed in some MORBs [e.g., *Zhao et al.*, 2006] and is attributed to inversion of a small fraction of titanomaghemite. The higher temperature phase with $T_c \approx 580$°C is the hallmark of the occurrence of magnetite.

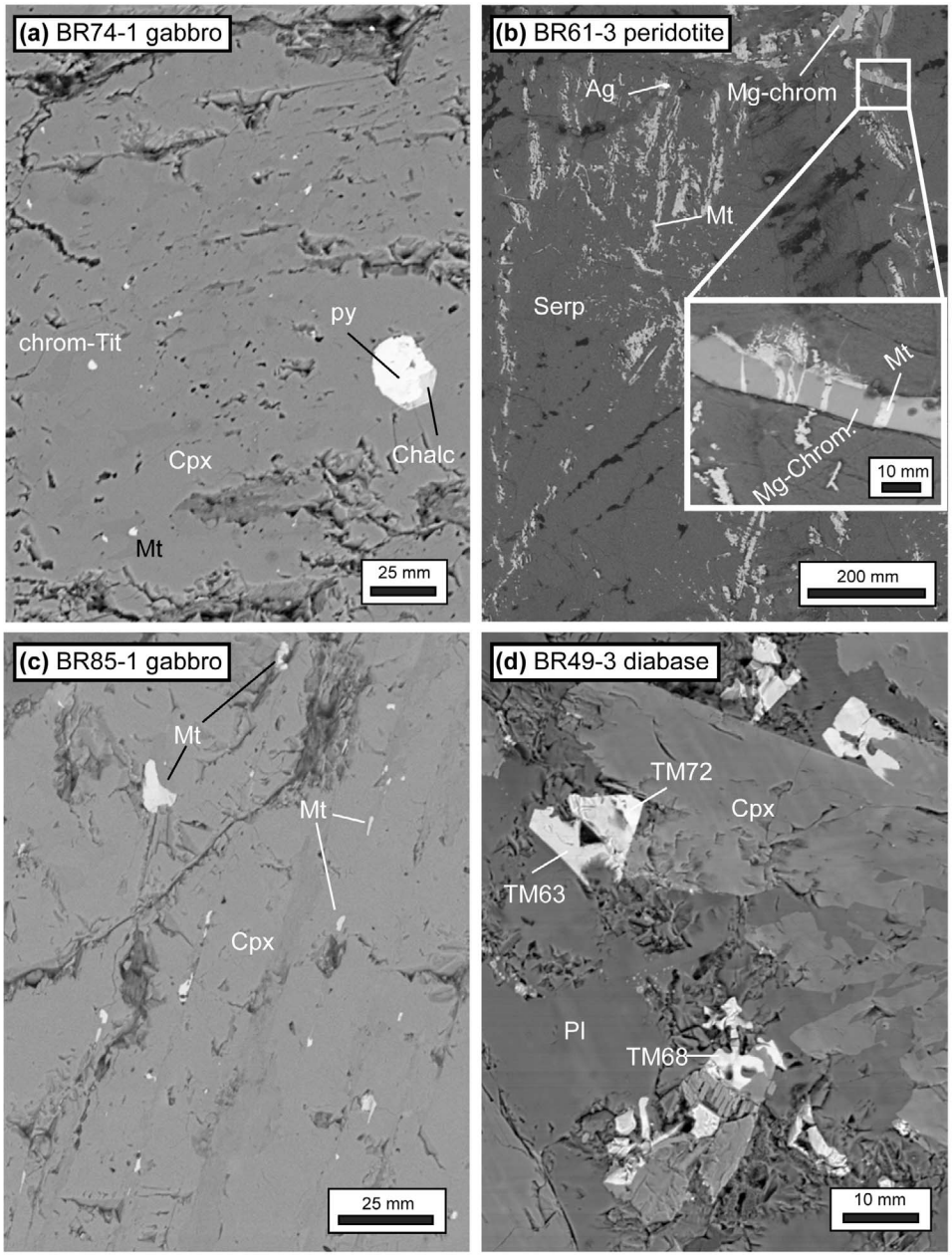

Figure 9. (a) SEM image of olivine-bearing gabbro BR74-1. Small magnetites in between bigger minerals are common. In this image magnetite and titanium chromite occur in a cpx matrix; in addition, pyrite and chalcopyrite are found. (b) BR61-3 serpentinized peridotite. Very abundant magnetites with grain sizes of a few microns are clustered along veins in a serpentine matrix. Magnesian chromite grains are commonly observed in addition to magnetite (see also inset), as well as occasional metallic elements including silver. Sp, serpentine; Ag, silver; Mg-Chrom, magnesian chromite. (c) BR85-1 gabbro. Iron oxides are observed only rarely, and their distribution is very inhomogeneous. Magnetites are sometimes present along some fractures in clinopyroxene, and a few ilmenite grains are also present. (d) BR49-3 diabase. Numerous titanomagnetite with dendritic structure are present; smaller magnetites and pyrite-chalcopyrite (on the order or less of 1 μm) are also common.

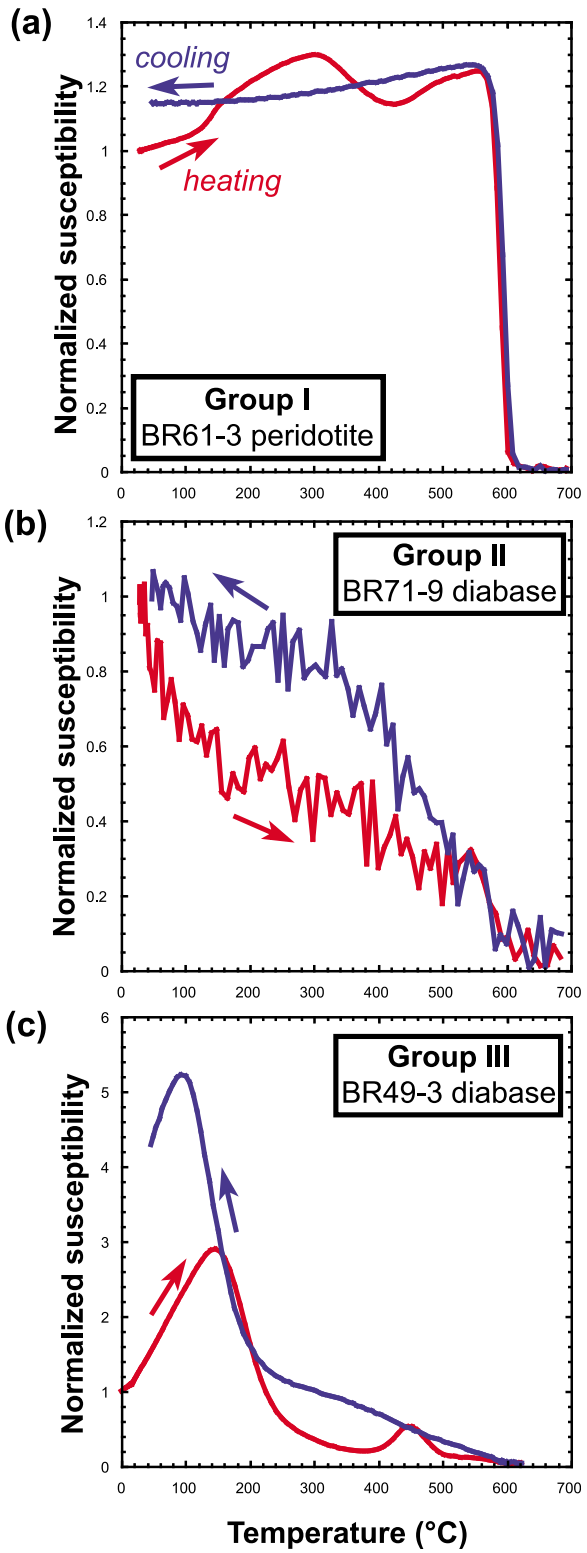

Figure 10. (a–c) Examples of typical thermomagnetic experiment results for the three groups with distinct magnetic characteristics as discussed in the text.

[45] An example of samples from the second group (Group II) is shown in Figure 10b. Samples belonging to this group are mostly diabase (BR71, BR31, BR79, BR76, BR35, BR87) and one gabbro (BR74). These samples show a weaker susceptibility signal (on the order of 1×10^{-7} m^3 kg^{-1}), measurements are noisy and show a large spectrum of unblocking temperatures upon heating. A magnetic fraction with unblocking temperature in the 580°–590°C range dominates the signal. In some cases the cooling curves are slightly above the heating curves. The magnetization of these samples is carried by a weak fraction of magnetite; irreversibility in some cases demonstrating the creation of magnetite during heating perhaps after inversion of a fraction of (titano)maghemite, or alteration of pyrite.

[46] A third type of behavior (Group III; Figure 10c) is observed in only two samples, both diabase. These are characterized by susceptibility around 5×10^{-6} m^3 kg^{-1} and show thermomagnetic curves with a first Curie point in the 200°C range (very pronounced for BR49, less so for BR75) and then an increase in the 350°C–450°C range. The cooling curve is irreversible, with a phase having a Curie point around 580°C for BR75 and an assemblage of phases with a Curie point at 580°C and another at 180°C for BR49. Such thermomagnetic curves are commonly observed in oceanic basalts [e.g., *Zhao et al.*, 2006] and probably reflect the inversion of titanomaghemite to magnetite during heating.

4.2.6. Inferred Magnetic Carriers

[47] Thermomagnetic results, demagnetization spectra and EDS-X analyses show that magnetite is the main magnetic carrier of magnetization, except for BR49 and BR75 in which titanomagnetite is present in significant amounts. In the samples belonging to thermomagnetic group I another phase could participate, as revealed by the rise of susceptibility in the ~120–340°C range (see Figure 10a). Nearly half of the analyzed samples and all peridotites belong to this group. During our SEM investigations we observed members of the chromite solid solution series in all peridotites but also in some gabbros. Other studies have reported such minerals in submarine gabbros and serpentinites (see in particular *Dunlop and Prevot* [1982] and more recently *Blackman et al.* [2006]). Chromites are possible carriers of remanent magnetization depending on the Cr and minor element content, and unblocking temperatures as high as 260°C have been reported [*Yu et al.*, 2001]. Iron sulfides were also sometimes

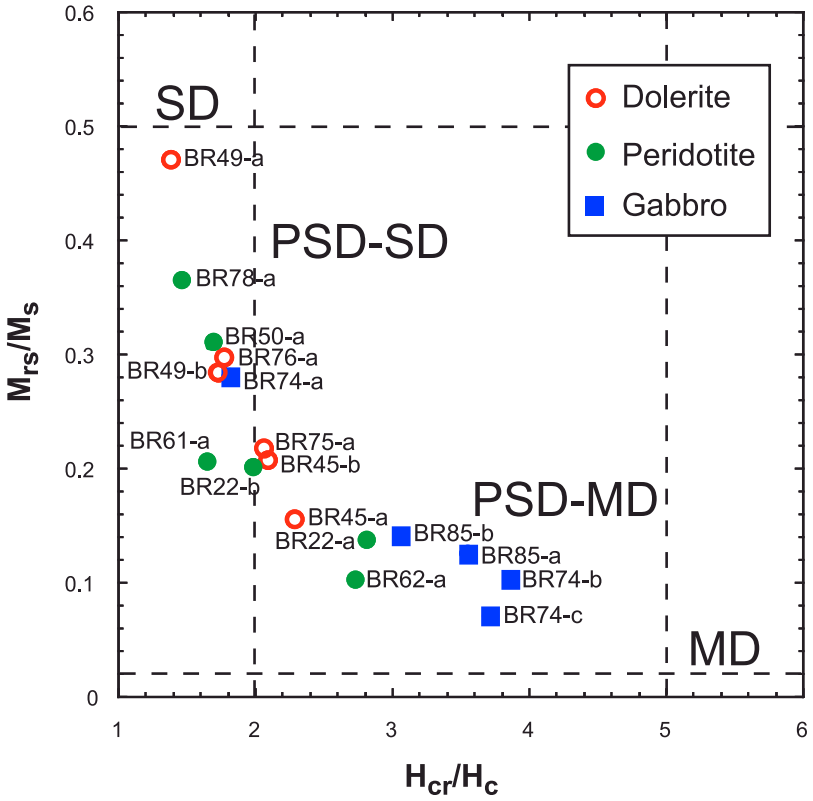

Figure 11. Hysteresis results on a Day plot [*Dunlop*, 2002]. SD, single domain; PSD, pseudo single domain; MD, multidomain. The dashed lines delimit the main ranges after *Dunlop* [2002] and should be seen only as approximate.

spotted during our SEM observations and could be candidates as magnetic carriers. Pyrrhotite, with a Curie point in the 270–320°C range, carries a remanence [e.g., *Crouzet et al.*, 2001]. The increase in susceptibility between 120°C and 340°C on the heating curve and its subsequent absence on cooling for thermomagnetic group I samples may thus reflect the transformation of pyrrhotite and/or chromite during heating to a phase assemblage that includes iron oxides.

[48] Since we demonstrated that pyrrhotite and/or chromite series minerals are possible magnetic carriers in some of our samples the influence of these phases on the primary directions has to be examined. Indeed, for all samples from Group I thermal demagnetization diagrams do not allow us to rule out a slight contribution from a phase with a lower unblocking temperature phase, in the 200–340°C range. However, in all cases the direction of magnetization is nearly constant throughout the greater part of the temperature spectrum, demonstrating the negligible effect of such a phase in the final direction determination. A typical example is given in Figure 7c by peridotite sample BR78. About half of the NRM is lost during demagnetization from 180°C to 330°C, and part of the magnetic signal could be carried by a low unblocking temperature phase; however, in this temperature interval the magnetization is in the same direction as the primary magnetization carried by magnetite in the higher temperature range.

[49] This result implies that the magnetic signal carried by a low unblocking temperature phase was apparently acquired prior to any rotation and probably during serpentinization. Serpentinization in peridotites from the 15°N area is thought to have started at ≤350°C and become widespread at temperatures at or below 250°C [*Bach et al.*, 2004]; therefore it is likely that most magnetite and other magnetic phases were formed, and their magnetic signals locked in, in this temperature range.

4.2.7. Hysteresis Measurements

[50] Hysteresis data from fragments of samples BR74 and BR85 (gabbro), BR22, BR50, BR61, BR62 and BR78 (peridotite), BR45, BR49, BR75 and BR76 (diabase) are shown in Figure 11. Samples yield values of saturation magnetization (M_s), saturation remanence (M_{rs}), coercive force (H_c), and

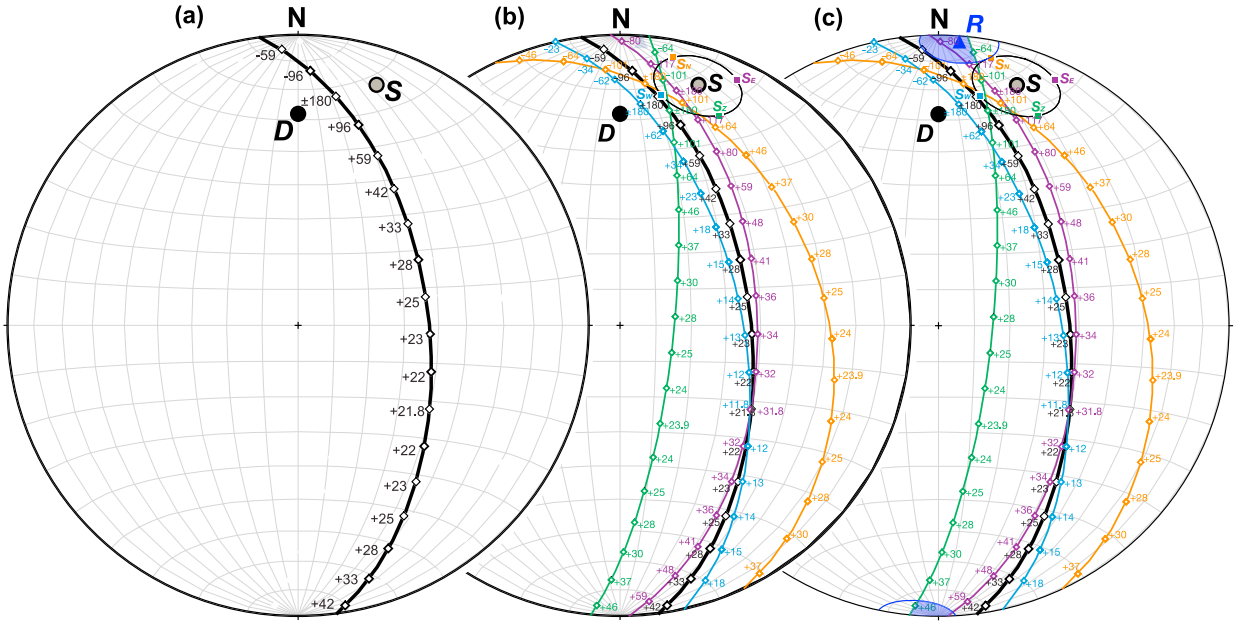

Figure 12. (a) The axes that can rotate the GAD direction *D* to *S*, the mean vector of stable remanences from the footwall of the 15°45′N OCC, are constrained to lie on a great circle bisectrix between the two. The variation in magnitude required to effect the rotation is shown by the figures calculated at 10° increments along the plane. Positive values indicate clockwise rotations, and negative values indicate counterclockwise rotations. (b) Same as Figure 12a but including permissible rotation axes and magnitudes for four additional points, S_N, S_E, S_Z, and S_W, that fall at the periphery of the 10° α_{95} cone of confidence around S. (c) Same as Figure 12b but shaded blue region is the area of intersection between the rotation axes inferred from the kinematic data in Figure 6 and axes permitted by the paleomagnetic data and hence inferred to be the (only) geologically realistic solutions.

remanent coercivity (H_{cr}) mostly in the pseudo-single-domain (PSD) grain size area of the Day plot [*Day et al.*, 1977; *Dunlop*, 2002]. The lower M_{rs}/M_s values from the two gabbro samples indicates larger grain size, near the multidomain (MD) range; however, the inhomogeneity in this material is shown by the rather different values found for one of the BR74 fragments (BR74-a) which are instead compatible with a magnetic grain size distribution in the PSD/SD range. Dolerite and serpentinized peridotites give values compatible with lower grain size in the PSD/SD range.

5. Geometrical Analysis of Rotations

[51] We here use the paleomagnetic and fault kinematic data above from the JR63 oriented core material (eight sites) in combination to analyze the rotation of the footwall of the 15°45′N. In this section we focus on the methodology and error analysis; in section 6 we discuss the geological implications of the results of the analysis.

[52] When only the vertical components of two directions are known, as with azimuthally unoriented (ODP-type) core samples, the number of solutions that can give rise to the measured change in inclination is infinite. When the horizontal component is also known, as here, the permissible solutions are constrained to lie on a great circle equidistant between the two vectors *S* (mean sample vector) and *D* (GAD; Figure 12). The magnitudes of rotation that take *D* to *S* vary progressively along this plane, from a minimum of +21.8° (clockwise) about a point perpendicular to both *S* and *D*, to a maximum of ±180° about the point on the plane closest to *S* and *D* (Figure 12). However, the paleomagnetic data in themselves give no further constraint upon the actual rotation that occurred, and additional criteria are needed to determine which of the permissible axes shown in Figure 12 is most plausible. From Figure 12 it can be seen that the most apparently reasonable a priori assumptions (as made in all previous studies), that the rotation axis should be horizontal and parallel either to the strike of the ridge (here 000°) or perpendicular to the spreading direction (276° [*Sella et al.*, 2002]), are not strictly permitted for *S* in this case. Rotation axes with these azimuths must plunge northward, and the magnitudes of rotation about 000° and 006° trending axes

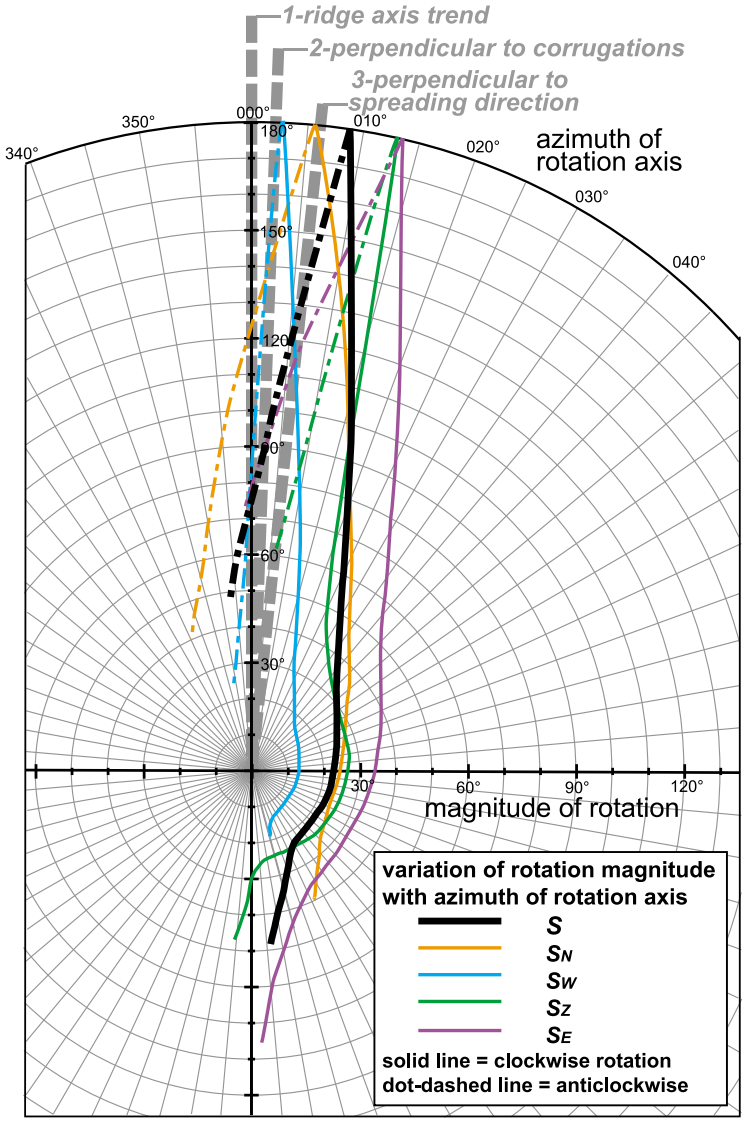

Figure 13. Polar plot showing the variation in rotation magnitude with azimuths of rotation axes calculated in Figure 12, demonstrating the sensitivity of the calculated magnitude of rotation to the axis chosen. Axis 1 is the mean trend of the ridge axis, axis 2 is the perpendicular to the corrugations on the 15°45′N OCC surface, and axis 3 is the perpendicular to the spreading direction (gray dashed lines). For the potential axes that can rotate D to S (thick black line) the inferred magnitude of rotation varies from −75° to −130° depending on whether axis 1, 2, or 3 is chosen a priori. If the uncertainty in the mean magnetization vector S is also considered (colored lines, as in Figure 12b), the nonuniqueness and extreme uncertainty of the solution for any one of the possible "geologically reasonable" rotation azimuths becomes apparent.

are ~75° and ~130° counterclockwise, respectively (Figure 13). The significant disparity between these figures demonstrates how exceptionally sensitive the magnitude of rotation is to the azimuth of the axis chosen, especially if (as here) this axis is believed to lie between S and D, and illustrates the danger of inferring quantitative magnitudes of rotation with incomplete geometrical information.

[53] The situation is exacerbated when the 10° uncertainty in the mean remanence direction S is considered: shown here by calculating rotation axes and magnitudes for four additional points S_W, S_N, S_E and S_Z that lie at the edges of the α_{95} cone of confidence (thereby defining the envelope containing all possible rotation axes; Figure 12b). The precise topology of the resulting solutions that rotate S_W, S_N, S_E and S_Z as well as S to D is complex: a plethora of solutions, with widely differing magnitudes of rotation, is possible even for the same axis (Figure 12b). This demonstrates that paleomagnetic

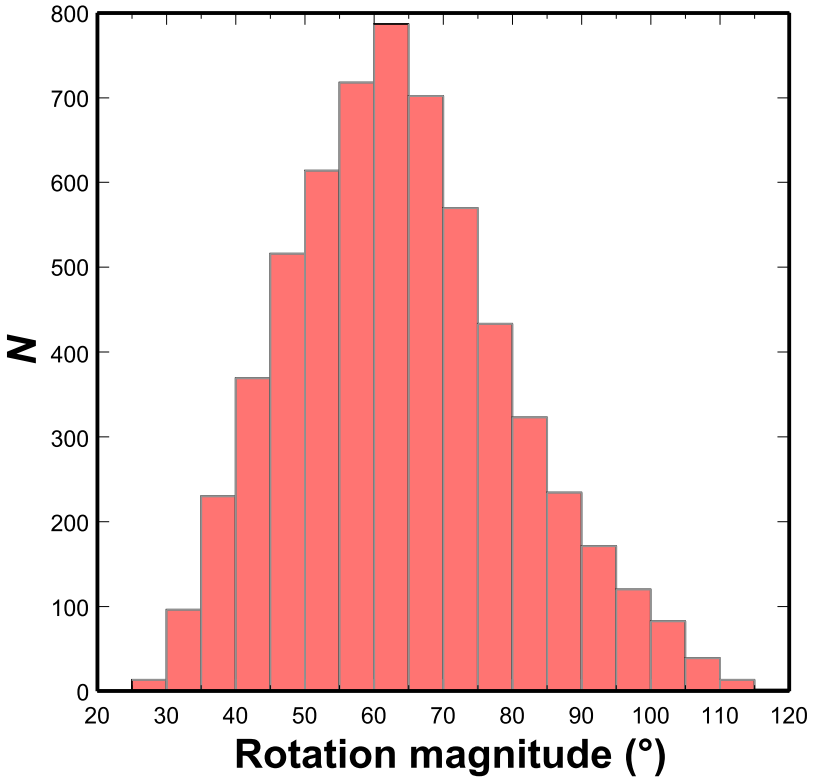

Figure 14. Frequency distribution of resultant rotation magnitudes inferred from Monte Carlo modeling. See text for discussion.

data even from fully oriented cores cannot uniquely constrain either the axis or magnitude of rotation, unless additional, external information is available.

[54] The most direct constraint possible on the actual rotation axis should come from knowledge of the kinematics of the geological structures directly responsible for the rotation. All models for the origin and unroofing of OCCs, whether assuming curved or planar detachment faults, hold that the massifs are exhumed as a direct result of motion on the detachment surfaces. Consequent rotations ought therefore to be recorded in the kinematic history of fault rocks on the detachment surface itself. Any subsequent, unrelated rotations are likely to affect the paleomagnetic and detachment fault zone kinematic data equally, leaving their relative angular relationship unchanged.

[55] The orientations (in true geographical coordinates) of foliation planes and associated lineations in the schistose fault rocks from the 15°45′N corrugated surface described in section 6 above are shown in Figure 6. In it we also plot the "no-slip" vector *R*, the perpendicular to the slickenside direction lying in the plane of the foliation, for each individual shear surface. If we make the geologically reasonable assumption that the high-strain schistose talc-tremolite-chlorite fault rocks on the surface of the 15°45′N OCC are responsible for accommodating any tilting that might have affected the footwall, the mean no-slip vector should define the rotation axis. This mean vector *R* has an azimuth of 004.2°, plunge of 2.3° and α_{95} of 8.0° (k = 12). We believe that this is a robust estimate of the axis of rotation, as no later oblique faults have been documented in the vicinity of the 15°45′N OCC [*MacLeod et al.*, 2002; *Fujiwara et al.*, 2003; *Schroeder et al.*, 2007].

[56] In Figure 12c the mean rotation axis and associated cone of confidence defined from the kinematic data is shown together with the axes of rotation from the analysis of the uncertainties in the remanence direction data. Permissible axes of rotation lie where the two intersect (shaded in Figure 12c). To rigorously quantify the range of rotation magnitudes permitted for these solutions we conducted a Monte Carlo simulation, defining 1000 points S_r randomly distributed within the 10° cone of confidence about *S* and calculating rotation angles for poles distributed at 1° intervals around the full 360° of the bisectrix. This yields 360,000 potential solutions for each combination of S_r and *D*, of which some 6032 fall within the α_{95} confidence

cone about *R* and are therefore deemed geologically acceptable. Figure 14 shows the frequency distribution of rotation magnitudes thus calculated: mean and median (counterclockwise) rotations are 64.0° and 63.0°, respectively, with a standard deviation of 16.1° about the mean. The vector mean orientation of the 6032 solutions is 000.9°; 4.5° (α_{95} = 0.2°, k = 323), which is taken as the mean rotation axis.

6. Discussion: Geological Implications

6.1. Footwall Rotations at OCCs and Constraints on Subsurface Detachment Fault Geometry

[57] By analyzing stable magnetic remanence directions in oriented cores from the footwall of the 15°45′N OCC in conjunction with kinematic information derived from the high-strain fault rocks from its surface we have demonstrated that substantial tectonic rotation, of 64° ± 16°, of the footwall of the 15°45′N OCC has occurred, and that this rotation was effected about a gently plunging, near-ridge-parallel axis (azimuth 000.9°, plunge 4.5°).

[58] In detail, we note that the 64° ± 16° magnitude figure we obtain is the total accumulated rotation suffered by the OCC, and potentially includes a component accommodated on the termination fault at the eastern (ridgeward) margin of the massif at 46°52′/46°53′W (section 2.3 and Figure 3) as well as that taken up by the oceanic detachment fault itself. *Cannat et al.* [2009] posit that relatively elevated topography of certain OCC massifs is acquired immediately after activity on the detachment ceases and is accommodated by uplift of the footwall of the large, ridgeward dipping termination fault. We argue that for 15°45′N any such late back tilt, which cannot be separately resolved, must have occurred about an identical, or near-identical, axis to that of the main detachment and was of much smaller magnitude: no more than 5° if the 1.4 km of throw on the termination fault accommodated pivoting of the 17 km wide corrugated surface.

[59] Overall, therefore, we conclude that the principal, high-strain detachment fault zone exposed on the corrugated surface of the 15°45′N OCC accommodated all or almost all of the 64° ± 16° documented rotation. This result is entirely consistent with, and offers strong support for, the rolling hinge class of models for oceanic detachment faulting [e.g., *Lavier et al.*, 1999; *Buck et al.*, 2005; *Tucholke et al.*, 2008], in which flattening and rollover of initially steep, Andersonian normal faults occurs in response to plate flexure upon unloading of the hanging wall.

[60] By this analysis we robustly confirm the supposition proposed on the basis of inclination-only [*Garcés and Gee*, 2007; *Zhao and Tominaga*, 2009] and reoriented ODP/IODP paleomagnetic data [*Morris et al.*, 2009] from sites at the MAR. This finding does apparently contrast with the 17 to 20° magnitude rotation inferred from the footwall of the Atlantis Bank detachment fault on the SW Indian Ridge [*Pariso et al.*, 1991; *Pettigrew et al.*, 1999; *Dick et al.*, 2000; *Allerton and Tivey*, 2001]; however, the Atlantis Bank OCC is very different from those on the MAR, being dominated by plastically deformed gabbros, and we suggest in this instance that much of the rotation of the plutonic section occurred above the Curie temperature of the gabbros and was therefore not recorded paleomagnetically.

[61] The ODP/IODP results from the MAR to date have all been obtained from single boreholes or sites, and do not therefore strictly constrain the scale or consistency of block rotation on the scale of an OCC. Potentially, therefore, the documented rotations might be only local in scale, and could perhaps have been accommodated on several different faults acting either sequentially or in concert [e.g., *Nur et al.*, 1986]; therefore explained away as local geometrical complexities within a broader, essentially pure shear, planar or conjugate fault model. This argument can now, however, be discounted. Mean inclinations from ODP Holes 1275B (at −9.5°) and 1275D (at −6.5° to −13.4°) are within error of the −14° ± 10° envelope of the inclination of the mean sample magnetization vector found in the JR63 samples, and hence are consistent with a similar magnitude of rotation on the length scale equivalent to that of the boreholes (≥200 m into the footwall). More significantly, the similarity in magnetization directions in our eight separate footwall sites spaced a total of 11 km apart parallel to the spreading direction (Figure 4) implies that rotations are consistent on the scale of the entire OCC and therefore persisted, about similar axes and magnitudes, for at least 0.8 Myr of activity on the detachment fault.

[62] It is geologically unreasonable to conclude that the entire OCC rotated all at the same time as one single, rigid block. Instead, the above observation implies that all parts of the footwall (or at least those adjacent to the detachment fault itself) successively experienced a similar cumulative rotational strain during their exhumation onto the seafloor. Geometrically, rotation of the magnitude documented at

the 15°45′N OCC can be accommodated on a single, essentially continuous structure in this manner only if the fault itself has a curved, convex-downward "antilistric" geometry. In keeping with the simple conceptual models [e.g., *Buck*, 1988; *Wernicke and Axen*, 1988; *Lavier et al.*, 1999] the observations are entirely consistent with a scenario in which the fault is flattened by rotation above a fixed "rolling hinge" and its inactive portion extruded onto the seafloor while activity on the steep portion of the fault continues at depth.

[63] The original steep, ridgeward dipping ridge-parallel orientation of the structure at 15°45′N is demonstrated by the restoration of foliations in the fault schists, and of the corrugated surface, to their pretilting configurations: rotating the data by the mean axis and magnitude derived in section 5 yields an initial strike of 004° and dip of 60° east for the fault rocks and 003° strike and 62° east dip for the OCC surface. These figures are not affected by the estimates of the proportion of rotation accommodated by late back tilting discussed above. A steep, ridge-parallel geometry of initiation (65 ± 10°) is likewise deduced for active OCC detachment faults in the 13°N region of the MAR on the basis of the angular relationship between tilted volcanic surfaces and fault planes there [*MacLeod et al.*, 2009].

[64] What is less easy to constrain is the depth and radius of curvature of rollover of the detachment faults. At 15°45′N curvature of the exhumed fault plane is observed in the slight convex upward shape of the western knolls of the OCC (Figure 3). Some of the OCCs in the 13°N region (e.g., at 13°19′/13°20′N) may display prominent, convex-upward curvature of their exposed, inactive portions [*Smith et al.*, 2006, 2008; *MacLeod et al.*, 2009]. Convex-upward curvature of the OCC surface is also evident at the Atlantis Massif (MAR 30°N) [e.g., *Cann et al.*, 1997]. It is not necessarily the case, though, that the radius of curvature seen at the surface is constant and can be extrapolated subsurface [*MacLeod et al.*, 2009].

[65] The best constraint on the subsurface depth and radius of curvature of a detachment probably comes from the TAG region [*deMartin et al.*, 2007], but even here the locus of rollover is not observed directly. Although the microearthquake hypocenters clearly define a steeply dipping (~70°) structure from 7 km to ~3 km below seafloor, uniform in dip but varying in strike, convex in the direction of the spreading axis, earthquakes are not recorded at shallower depths. As a result *deMartin et al.* [2007] were obliged instead to infer that the steeply dipping seismogenic fault is linked to an aseismic interface, identified on the basis of seismic tomography, that dips at ~20° toward the spreading axis from 3 km depth up to the seafloor, where it links with an exposed scarp of similar orientation. Although the evidence is therefore indirect, it is consistent with a tight radius of curvature and rapid, near-surface rollover of the fault in this instance.

[66] It may nevertheless be concluded that the observed radii of curvature of the exposed parts of OCCs, taken with the observation that virtually all of the flattening of the fault plane (and hence rotation of the footwall) must already have been accommodated by the time it appears at the seafloor [*MacLeod et al.*, 2009], implies that the newly created lithosphere within and immediately adjacent to and on the OCC side of the ridge axis has extremely low flexural rigidity. *Smith et al.* [2008] and *Schouten et al.* [2010] estimate that elastic thicknesses may be as low as ~0.5–1 km, increasing rapidly away from the axis.

[67] Whereas we conclude that the convex-upward curvature inferred at 15°45′N, TAG and other OCCs is likely to be a general feature for most oceanic detachment faults, the actual depth of rollover and radius of curvature do not appear to be the same everywhere. The corrugated surface at the Atlantis Massif at 30°N on the MAR preserves a basaltic rider block on its upper surface, between it and the axial valley [*Cann et al.*, 1997; *Blackman et al.*, 2006], and *Dannowski et al.* [2010] infer several such hanging wall klippen at the MAR at 22°N. TAG is probably similar. In these cases the detachment fault appears to roll over at a greater depth and/or with greater radius of curvature than those where the detachment emerges directly at the edge of the axial valley, as for example in the 13°N region [*Smith et al.*, 2006; *MacLeod et al.*, 2009]. Such differences may reflect variations in effective elastic thickness, perhaps arising from different thermal structures in the axial lithosphere, or from differing extents of weakening of the footwall.

6.2. Origin of Diabase Intrusions in the 15°45′N Massif

[68] Crosscutting relationships preserved in the BRIDGE drill cores demonstrate that intrusion of the diabase bodies bracketed the period of activity on the 15°45′N detachment fault (sections 2.3 and 4.1). We can constrain the origin of these intrusions by restoring the chilled margins of these bodies to their original, prerotation orientations.

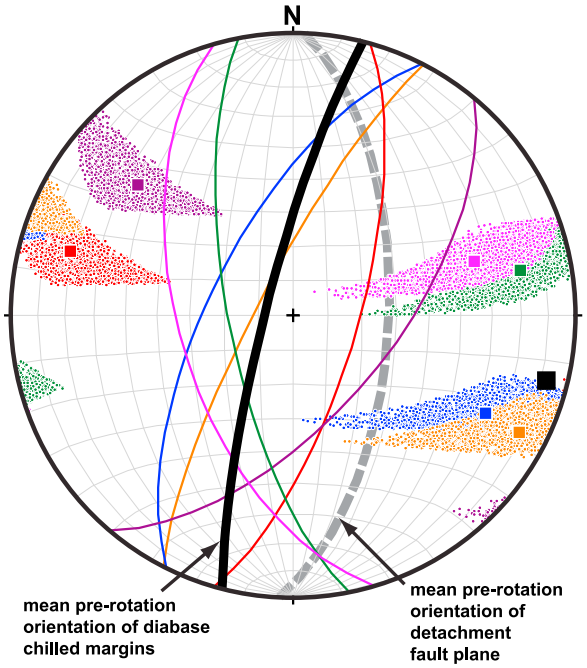

Figure 15. Equal area stereographic projection of the orientations of six chilled diabase margins reoriented by the geologically permissible solutions derived from the Monte Carlo modeling. Medium-sized colored squares are the mean of the 6032 possible poles to planes of each chilled margin, and lines are the great circles of mean planes. The large black square and line represent the mean pole and plane, respectively, for the six bodies. The near-vertical, approximately N-S orientations of the reoriented chilled margins demonstrate that these diabase bodies were originally part of a ridge-parallel dike swarm. The gray dashed line represents the original, prerotation orientation of the corrugated detachment fault plane, which lies at an angle of 38° from the mean dike trend.

Applying the rotation axes and (inverse) magnitudes of the 6032 geologically acceptable solutions found in section 5 to each of six planar, undeformed, chilled diabase margins measured in the JR63 cores, we find that their current shallow dip angles restore to a mean original dip of 82° west and strike of 014°: i.e., almost vertical, and very close to the trend of the MAR spreading axis (Figure 15). This demonstrates convincingly that the intrusions were originally ridge-parallel dikes, either sheeted or with serpentinized peridotite screens between dikes, rather than a set of sills or detachment-parallel intrusions as postulated for similar diabase bodies at Site U1309 (MAR 30°N) [*Blackman et al.*, 2006; *McCaig et al.*, 2010]. An angular difference of ~38° between the mean dike trend and original fault orientation means that the dike swarm was intruded across the detachment fault rather than up and along it (Figure 15). These dikes (locally sheeted) are likely therefore to have contributed to a magmatic component of plate separation and to have delivered extrusive products to the hanging wall of the detachment [*MacLeod et al.*, 2009].

6.3. Implications for the Thermal Structure of OCCs

[69] Because of the near absence of high-temperature crystal-plastic deformation in the footwall gabbro and predominance of low-temperature greenschist facies (talc–tremolite ± chlorite) assemblages in the fault zone, we originally suggested [*MacLeod et al.*, 2002; *Escartín et al.*, 2003] that 15°45′N detachment fault must have soled out at a relatively shallow level in the lithosphere. However, because we have now determined in this paper that the detachment fault had a steepening downward subsurface geometry, and was demonstrably initiated and active as a steep, ridge-parallel normal fault the argument may be inverted: we surmise that the P-T conditions recorded by the faults instead require rapid and efficient cooling to very deep levels, with embrittlement and strain weakening presumably taking place in a localized process zone at the base of the brittle lithosphere. Within this zone, at a probable depth of ~7–8 km (the maximum depth of microearthquakes on the MAR [e.g., *Toomey et al.*, 1985; *deMartin et al.*, 2007]), the detachment system cooled very rapidly, down to no more than 350–400°C, as a result of the channeling of hydrothermal fluids along it [*McCaig et al.*, 2007], at the same time leading to precipitation of talc and other phyllosilicates, and thence large-scale weakening and strain localization in consequence. *Escartín et al.* [2001] and *Moore and Lockner* [2011] have demonstrated that even small amounts of alteration (10%–15% serpentine or talc) on a fault plane can lead to wholesale weakening on a fault or whole-lithosphere scale. *Escartín et al.* [2008a] further showed that talc, which is stable to 700°C, has the potential to lubricate the fault to levels as deep as the brittle plastic transition. Isotherms are likely to have been deflected near to parallelism with the fault plane (analogous to those within a subducting slab) by the action of the hydrothermal fluid channeling and heat advection [see also *McCaig et al.*, 2010].

[70] Because our serpentinized peridotite samples from the OCC record the full tectonic rotation documented above, we further surmise that the footwall of the detachment, at least adjacent to the fault zone, must have already been serpentinized, prior to fault rollover, deep beneath the axial valley, and already

cooled to no higher than 200–350°C [e.g., *Bach et al.*, 2004; *Früh-Green et al.*, 2004]. It also indicates that fluid circulation in the footwall, at least in close proximity to the fault, is established early on and at deep levels. The consequential weakening of the peridotite footwall upon serpentinization and formation of talc [e.g., *Escartín et al.*, 1997, 2001, 2008a] at this early stage is likely to have played a significant role in helping accommodate the internal deformation of the footwall block and the establishment of the curvature of the fault that allowed rollover to take place. On a regional scale this probably contributes to the plate-scale weakening and low flexural rigidity of the OCC described above [e.g., *Cannat et al.*, 2009]. The early serpentinization, and hence weakening of the footwall relative to a mafic hanging wall, may in turn have promoted the formation of corrugations on the detachment fault by continuous casting of the soft altered footwall in a manner similar to that envisaged by *Spencer* [1999].

[71] The diabase dike swarm in the SE corner of the 15°45′N OCC was also intruded into this cooled, serpentinized lithospheric mantle footwall prior to rotation, apparently over a protracted interval continuing to less than 1.95 Myr ago. The spatial proximity of this dike swarm to the gabbro body that lies directly beneath suggest that the dikes are fed from it [*MacLeod et al.*, 2002; *Escartín et al.*, 2003]. Whereas our study does not directly constrain the depth, or more likely range of depths, over which the ≥10 × ≥ 5 × >1 km sized gabbro body in the SE corner of the 15°45′N OCC was emplaced into the detachment footwall, we can deduce that it was uplifted and incorporated into the brittle lithosphere almost immediately after crystallization, on the basis of the evolved composition of most of the gabbro, relatively finer grain size at the margin of the body [*Kelemen et al.*, 2004, 2007], and near absence of crystal-plastic deformation (implying that it cooled very rapidly through the temperature interval of gabbro ductility, of >~650°C).

[72] We suggest a scenario in which melt is emplaced into the lower lithosphere at or just below the 7–8 km maximum earthquake depth in the footwall immediately adjacent to a steeply dipping, active detachment fault. With ongoing uplift continuing melt emplacement leads to the construction of a composite gabbro pluton built by sill emplacement at its base, broadly similar to the mechanism inferred for Atlantis Massif [*Grimes et al.*, 2008]. This composite body is continually uplifted and rapidly cooled as slip proceeds on the weak, greenschist facies detachment fault. Swarms of dikes fed from the deeper interior of the uplifting gabbro body intrude outward and upward through the chilled gabbro roof zone into the adjacent serpentinized mantle lithosphere host, and into and across the detachment fault above. All of this takes place before any detectable rollover and rotation of the footwall/OCC, which appears therefore to occur at shallow depths immediately prior to exposure on the seafloor.

Acknowledgments

[73] We are indebted to C. Brett, J. Derrick, D. Smith, and D. Wallis from the British Geological Survey for their role in developing and operating the BRIDGE rock drill and the captain, crew, and science party of RRS *James Clark Ross* cruise JR63 for their role in collecting the cores analyzed herein. We thank the reviewers and Associate Editor for constructive comments on the manuscript. Funding from the Natural Environment Research Council is gratefully acknowledged. J.C. and J.E. were funded by CNRS/INSU.

References

Abers, G. A. (2009), Slip on shallow-dipping normal faults, *Geology*, *37*, 767–768, doi:10.1130/focus082009.1.

Abers, G. A., C. Z. Mutter, and J. Fang (1997), Shallow dips of normal faults during rapid extension: Earthquakes in the Woodlark-D'Entrecasteaux rift system, Papua New Guinea, *J. Geophys. Res.*, *102*, 15,301–15,317, doi:10.1029/97JB00787.

Allerton, S., and M. A. Tivey (2001), Magnetic polarity structure of the lower oceanic crust, *Geophys. Res. Lett.*, *28*, 423–426, doi:10.1029/2000GL008493.

Allerton, S., D. Wallis, J. Derrick, D. Smith, and C. J. MacLeod (1999), New wireline seafloor drill augers well, *Eos Trans. AGU*, *80*(33), 367.

Anderson, E. M. (1951), *The Dynamics of Faulting*, 206 pp., Oliver and Boyd, Edinburgh, U. K.

Bach, W., C. J. Garrido, H. Paulick, J. Harvey, and M. Rosner (2004), Seawater-peridotite interactions: First insights from ODP Leg 209, MAR 15°N, *Geochem. Geophys. Geosyst.*, *5*, Q09F26, doi:10.1029/2004GC000744.

Baines, A. G., M. J. Cheadle, H. J. B. Dick, A. Hosford Scheirer, B. E. John, N. J. Kusznir, and T. Matsumoto (2003), Mechanism for generating the anomalous uplift of oceanic core complexes: Atlantis Bank, southwest Indian Ridge, *Geology*, *31*, 1105–1108, doi:10.1130/G19829.1.

Berthé, D., P. Choukroune, and P. Jegouzo (1979), Orthogneiss, mylonite and non coaxial deformation of granites: The example of the South Armorican Shear Zone, *J. Struct. Geol.*, *1*, 31–42, doi:10.1016/0191-8141(79)90019-1.

Blackman, D. K., et al. (2002), Geology of the Atlantis Massif (Mid-Atlantic Ridge, 30°N): Implications for the evolution of an ultramafic oceanic core complex, *Mar. Geophys. Res.*, *23*, 443–469, doi:10.1023/B:MARI.0000018232.14085.75.

Blackman, D. K., B. Ildefonse, B. E. John, Y. Ohara, D. J. Miller, C. J. MacLeod, and Expedition 304/305 Scientists (2006), *Proceedings of the Integrated Ocean Drilling*

Program, vol. 304/305, doi:10.2204/iodp.proc.304305.101. 2006, Integrated Ocean Drill. Program, College Station, Tex.

Blackman, D. K., G. D. Karner, and R. C. Searle (2008), Three-dimensional structure of oceanic core complexes: Effects on gravity signature and ridge flank morphology, Mid-Atlantic Ridge, 30°N, *Geochem. Geophys. Geosyst.*, *9*, Q06007, doi:10.1029/2008GC001951.

Boschi, C., G. L. Früh-Green, and J. Escartín (2006), Occurrence and significance of serpentinite-hosted, talc- and amphibole-rich fault rocks in modern oceanic settings and ophiolite complexes: An overview, *Ofioliti*, *31*, 129–140.

Buck, W. R. (1988), Flexural rotation of normal faults, *Tectonics*, *7*, 959–973, doi:10.1029/TC007i005p00959.

Buck, W. R., L. L. Lavier, and A. N. B. Poliakov (2005), Modes of faulting at mid-ocean ridges, *Nature*, *434*, 719–723, doi:10.1038/nature03358.

Byerlee, J. D. (1978), Friction of rocks, *Pure Appl. Geophys.*, *116*, 615–626, doi:10.1007/BF00876528.

Campani, M., F. Herman, and N. Mancktelow (2010), Two- and three-dimensional thermal modeling of a low-angle detachment: Exhumation history of the Simplon Fault Zone, central Alps, *J. Geophys. Res.*, *115*, B10420, doi:10.1029/2009JB007036.

Canales, J. P., R. A. Sohn, and B. J. deMartin (2007), Crustal structure of the TAG segment (Mid-Atlantic Ridge, 26°10′N): Implications for the nature of hydrothermal circulation and detachment faulting at slow spreading ridges, *Geochem. Geophys. Geosyst.*, *8*, Q08004, doi:10.1029/2007GC001629.

Canales, J. P., B. E. Tucholke, M. Xu, J. A. Collins, and D. L. DuBois (2008), Seismic evidence for large-scale compositional heterogeneity of oceanic core complexes, *Geochem. Geophys. Geosyst.*, *9*, Q08002, doi:10.1029/2008GC002009.

Cann, J. R., D. K. Blackman, D. K. Smith, E. McAllister, B. Janssen, S. Mello, E. Avgerinos, A. R. Pascoe, and J. Escartín (1997), Corrugated slip surfaces formed at North Atlantic ridge-transform intersections, *Nature*, *385*, 329–332, doi:10.1038/385329a0.

Cannat, M., and J. F. Casey (1995), An ultramaphic lift at the Mid-Atlantic Ridge: Successive stages of magmatism in serpentinized peridotites from the 15°N region, in *Mantle and Lower Crust Exposed in Oceanic Ridges and in Ophiolites*, edited by R. L. M. Vissers and A. Nicolas, pp. 5–34, Kluwer Acad., Dordrecht, Netherlands.

Cannat, M., Y. Lagabrielle, H. Bougault, J. Casey, N. de Coutures, L. Dmitriev, and Y. Fouquet (1997), Ultramafic and gabbroic exposures at the Mid-Atlantic Ridge: Geological mapping in the 15°N region, *Tectonophysics*, *279*, 193–213, doi:10.1016/S0040-1951(97)00113-3.

Cannat, M., D. Sauter, J. Escartín, and S. Picazo (2009), Oceanic corrugated surfaces and the strength of the axial lithosphere at slow spreading ridges, *Earth Planet. Sci. Lett.*, *288*, 174–183, doi:10.1016/j.epsl.2009.09.020.

Cogné, J. P. (2003), Paleomac: A Macintosh application for treating paleomagnetic data and making plate reconstructions, *Geochem. Geophys. Geosyst.*, *4*(1), 1007, doi:10.1029/2001GC000227.

Crouzet, C., H. Stang, E. Appel, E. Schill, and P. Gautam (2001), Detailed analysis of successive pTRMs carried by pyrrhotite in Himalayan metacarbonates: An example from Hidden Valley, central Nepal, *Geophys. J. Int.*, *146*, 607–618, doi:10.1046/j.0956-540x.2001.01478.x.

Dannowski, A., I. Grevemeyer, C. R. Ranero, G. Ceuleneer, M. Maia, J. P. Morgan, and P. Gente (2010), Seismic structure of an oceanic core complex at the Mid-Atlantic Ridge, 22 degrees 19′N, *J. Geophys. Res.*, *115*, B07106, doi:10.1029/2009JB006943.

Day, R., M. Fuller, and V. A. Schmidt (1977), Hysteresis properties of titanomagnetites: Grain-size and compositional dependence, *Phys. Earth Planet. Inter.*, *13*, 260–267, doi:10.1016/0031-9201(77)90108-X.

deMartin, B. J., R. A. Sohn, J.-P. Canales, and S. E. Humphris (2007), Kinematics and geometry of active detachment faulting beneath the Trans-Atlantic Geotraverse (TAG) hydrothermal field on the Mid-Atlantic Ridge, *Geology*, *35*, 711–714, doi:10.1130/G23718A.1.

DeMets, C., R. G. Gordon, D. F. Argus, and S. Stein (1990), Current plate motions, *Geophys. J. Int.*, *101*, 425–478, doi:10.1111/j.1365-246X.1990.tb06579.x.

DeMets, C., R. G. Gordon, D. F. Argus, and S. Stein (1994), Effect of recent revisions to the geomagnetic reversal time scale on estimates of current plate motions, *Geophys. Res. Lett.*, *21*, 2191–2194, doi:10.1029/94GL02118.

Dick, H. J. B., et al. (2000), A long in situ section of the lower ocean crust: Results of ODP Leg 176 drilling at the Southwest Indian Ridge, *Earth Planet. Sci. Lett.*, *179*, 31–51, doi:10.1016/S0012-821X(00)00102-3.

Dunlop, D. J. (2002), Theory and application of the Day plot (M_{rs}/M_s versus H_{cr}/H_c) 1. Theoretical curves and tests using titanomagnetite data, *J. Geophys. Res.*, *107*(B3), 2056, doi:10.1029/2001JB000486.

Dunlop, D. J., and M. Prevot (1982), Magnetic properties and opaque mineralogy of drilled submarine intrusive rocks, *Geophys. J. R. Astron. Soc.*, *69*, 763–768.

Escartín, J., and M. Cannat (1999), Ultramafic exposures and the gravity signature of the lithosphere near the Fifteen-Twenty Fracture Zone (Mid-Atlantic Ridge, 14°–16.5°N), *Earth Planet. Sci. Lett.*, *171*, 411–424, doi:10.1016/S0012-821X(99)00169-7.

Escartín, J., G. Hirth, and B. Evans (1997), Effects of serpentinization on the lithospheric strength and the style of normal faulting at slow-spreading ridges, *Earth Planet. Sci. Lett.*, *151*, 181–189, doi:10.1016/S0012-821X(97)81847-X.

Escartín, J., G. Hirth, and B. Evans (2001), Strength of slightly serpentinized peridotites: Implications for the tectonics of oceanic lithosphere, *Geology*, *29*, 1023–1026, doi:10.1130/0091-7613(2001)029<1023:SOSSPI>2.0.CO;2.

Escartín, J., C. Mével, C. J. MacLeod, and A. M. McCaig (2003), Constraints on deformation conditions and the origin of oceanic detachments: The Mid-Atlantic Ridge core complex at 15°45′N, *Geochem. Geophys. Geosyst.*, *4*(8), 1067, doi:10.1029/2002GC000472.

Escartín, J., M. Andreani, G. Hirth, and B. Evans (2008a), Relationships between the microstructural evolution and the rheology of talc at elevated pressures and temperatures, *Earth Planet. Sci. Lett.*, *268*, 463–475, doi:10.1016/j.epsl.2008.02.004.

Escartín, J., D. K. Smith, J. R. Cann, H. Schouten, C. H. Langmuir, and S. Escrig (2008b), Central role of detachment faults in accretion of slow-spreading oceanic lithosphere, *Nature*, *455*, 790–794, doi:10.1038/nature07333.

Fisher, R. A. (1953), Dispersion on a sphere, *Proc. R. Soc. London, Ser. A*, *217*, 295–305, doi:10.1098/rspa.1953.0064.

Früh-Green, G. L., J. A. D. Connolly, and A. Plas (2004), Serpentinization of oceanic peridotites: Implications for geochemical cycles and biological activity, in *The Subseafloor Biosphere at Mid-Ocean Ridges*, *Geophys. Monogr. Ser.*, vol. 144, edited by W. S. D. Wilcock et al., pp. 119–136, AGU, Washington, D. C.

Fujiwara, T., J. Lin, T. Matsumoto, P. B. Kelemen, B. E. Tucholke, and J. F. Casey (2003), Crustal Evolution of the Mid-Atlantic Ridge near the Fifteen-Twenty Fracture Zone in the last 5 Ma, *Geochem. Geophys. Geosyst.*, *4*(3), 1024, doi:10.1029/2002GC000364.

Garcés, M., and J. S. Gee (2007), Paleomagnetic evidence of large footwall rotations associated with low-angle faults at the Mid-Atlantic Ridge, *Geology*, *35*, 279–282, doi:10.1130/G23165A.1.

Grimes, C. B., B. E. John, M. J. Cheadle, and J. L. Wooden (2008), Protracted construction of gabbroic crust at a slow-spreading ridge: Constraints from $^{206}Pb/^{238}U$ zircon ages from Atlantis Massif and IODP Hole U1309D (30°N, MAR), *Geochem. Geophys. Geosyst.*, *9*, Q08012, doi:10.1029/2008GC002063.

Hreinsdottir, S., and R. A. Bennett (2009), Active aseismic creep on the Alto Tiberina low-angle normal fault, Italy, *Geology*, *37*, 683–686, doi:10.1130/G30194A.1.

Ildefonse, B., D. K. Blackman, B. E. John, Y. Ohara, D. J. Miller, C. J. MacLeod, and the Integrated Ocean Drilling Program Expeditions 304/305 Science Party (2007), Oceanic core complexes and crustal accretion at slow-spreading ridges, *Geology*, *35*, 623–626, doi:10.1130/G23531A.1.

John, B. (1987), Geometry and evolution of a midcrustal extension fault system: Chemehuevi Mountains, southeastern California, in *Continental Extensional Tectonics*, edited by M. P. Coward et al., *Spec. Publ. Geol. Soc. London*, *28*, 313–335.

John, B. E., and D. A. Foster (1993), Structural and thermal constraints on the initiation angle of detachment faulting in the southern Basin and Range: The Chemehuevi Mountains case study, *Geol. Soc. Am. Bull.*, *105*, 1091–1108, doi:10.1130/0016-7606(1993)105<1091:SATCOT>2.3.CO;2.

Karson, J. A. (1990), Seafloor spreading on the Mid-Atlantic Ridge: Implications for the structure of ophiolites and oceanic lithosphere produced in slow-spreading environments, in *Ophiolites and Oceanic Crustal Analogues: Proceedings of the Symposium "Troodos 1987*," edited by J. Malpas et al., pp. 125–130, Geol. Surv. Dep., Nicosia, Cyprus.

Karson, J. A., G. L. Früh-Green, D. S. Kelley, E. A. Williams, D. R. Yoerger, and M. Jakuba (2006), Detachment shear zone of the Atlantis Massif core complex, Mid-Atlantic Ridge, 30°N, *Geochem. Geophys. Geosyst.*, *7*, Q06016, doi:10.1029/2005GC001109.

Kelemen, P. B., et al. (2004), *Proceedings of the Ocean Drilling Program, Initial Reports*, vol. 209, doi:10.2973/odp.proc.ir.209.2004, Ocean Drill. Program, College Station, Tex.

Kelemen, P. B., E. Kikawa, D. J. Miller, and Shipboard Scientific Party (2007), Leg 209 summary: Processes in a 20-km-thick conductive boundary layer beneath the Mid-Atlantic Ridge, 14°–16°N, *Proc. Ocean Drilling Program Sci. Results*, *209*, 1–33, doi:10.2973/odp.proc.sr.209.001.2007.

Kirschvink, J. (1980), The least-squares line and plane and the analysis of paleomagnetic data: Examples from Siberia and Morocco, *Geophys. J. R. Astron. Soc.*, *62*, 699–718.

Lagabrielle, Y., D. Bideau, M. Cannat, J. A. Karson, and C. Mével (1998), Ultramafic-mafic plutonic rock suites exposed along the Mid-Atlantic Ridge (10°N–30°N). Symmetrical-asymmetrical distribution and implications for seafloor spreading processes, in *Faulting and Magmatism at Midocean Ridges*, *Geophys. Monogr. Ser.*, vol. 106, edited by W. R. Buck et al., pp. 153–176, AGU, Washington, D. C.

Lavier, L. L., W. R. Buck, and A. N. B. Poliakov (1999), Self-consistent rolling-hinge model for the evolution of large-offset low-angle normal faults, *Geology*, *27*, 1127–1130, doi:10.1130/0091-7613(1999)027<1127:SCRHMF>2.3.CO;2.

Lecomte, E., L. Jolivet, O. Lacombe, Y. Denèle, L. Labrousse, and L. Le Pourhiet (2010), Geometry and kinematics of Mykonos detachment, Cyclades, Greece: Evidence for slip at shallow dip, *Tectonics*, *29*, TC5012, doi:10.1029/2009TC002564.

MacLeod, C. J., L. M. Parson, W. W. Sager, and the ODP Leg 135 Scientific Party (1992), Identification of tectonic rotations in boreholes by the integration of core information with Formation MicroScanner and Borehole Televiewer images, in *Geological Applications of Wireline Logs II*, edited by A. Hurst et al., *Spec. Publ. Geol. Soc. London*, *65*, 235–246.

MacLeod, C. J., L. M. Parson, and W. W. Sager (1994), Reorientation of core using the Formation MicroScanner and Borehole Televiewer: Application to structural and palaeomagnetic studies with the Ocean Drilling Program, *Proc. Ocean Drill. Program Sci. Results*, *135*, 301–311.

MacLeod, C. J., B. Célérier, and P. K. Harvey (1995), Further techniques for core reorientation by core-log integration: Application to structural studies of lower oceanic crust in Hess Deep, eastern Pacific, *Sci. Drill.*, *5*, 77–86.

MacLeod, C. J., et al. (2002), Direct geological evidence for oceanic detachment faulting: The Mid-Atlantic Ridge, 15°45′N, *Geology*, *30*, 879–882, doi:10.1130/0091-7613(2002)030<0879:DGEFOD>2.0.CO;2.

MacLeod, C. J., R. C. Searle, B. J. Murton, J. F. Casey, C. Mallows, S. C. Unsworth, K. L. Achenbach, and M. Harris (2009), Life cycle of oceanic core complexes, *Earth Planet. Sci. Lett.*, *287*, 333–344, doi:10.1016/j.epsl.2009.08.016.

Matsumoto, T., P. B. Kelemen, and MODE'98 Leg 1 Scientific Party (1998), Precise geological and geophysical mapping of the 15°20′N Fracture Zone on the MAR—Tectonic extension and its consequent exposure of ultramafic and plutonic rocks along the magma-poor ridge axis (MODE'98 Leg 1 Cruise), *InterRidge Newsl.*, *7*, 13–17.

McCaig, A. M., B. Cliff, J. Escartín, A. E. Fallick, and C. J. MacLeod (2007), Oceanic detachment faults focus very large volumes of black smoker fluids, *Geology*, *35*, 935–938, doi:10.1130/G23657A.1.

McCaig, A. M., A. Delacour, A. E. Fallick, T. Castelain, and G. L. Früh-Green (2010), Detachment fault control on hydrothermal circulation systems: Interpreting the subsurface beneath the TAG hydrothermal field using the isotopic and geological evolution of oceanic core complexes in the Atlantic, in *Diversity of Hydrothermal Systems on Slow Spreading Ocean Ridges*, *Geophys. Monogr. Ser.*, vol. 188, edited by P. A. Rona et al., pp. 207–240, AGU, Washington, D. C.

Moore, D. E., and D. A. Lockner (2008), Talc friction in the temperature range 25°C–400°C: Relevance for fault zone weakening, *Tectonophysics*, *449*, 120–132, doi:10.1016/j.tecto.2007.11.039.

Moore, D. E., and D. A. Lockner (2011), Frictional strengths of talc-serpentine and talc-quartz mixtures, *J. Geophys. Res.*, *116*, B01403, doi:10.1029/2010JB007881.

Morris, A., J. S. Gee, N. Pressling, B. E. John, C. J. MacLeod, C. B. Grimes, and R. C. Searle (2009), Footwall rotation in an oceanic core complex quantified using reoriented Integrated Ocean Drilling Program core samples, *Earth Planet. Sci. Lett.*, *287*, 217–228, doi:10.1016/j.epsl.2009.08.007.

Nur, A., H. Ron, and O. Scotti (1986), Fault mechanics and the kinematics of block rotations, *Geology*, *14*, 746–749, doi:10.1130/0091-7613(1986)14<746:FMATKO>2.0.CO;2.

Pariso, J. E., J. H. Scott, E. Kikawa, and H. P. Johnson (1991), A magnetic logging study of Hole 735B gabbros at the Southwest Indian Ridge, *Proc. Ocean Drill. Program Sci. Results*, *118*, 309–321, doi:10.2973/odp.proc.sr.118.149.1991.

Pettigrew, T. L., et al. (1999), *Proceedings of the Ocean Drilling Program, Initial Reports*, vol. 179, doi:10.2973/odp.proc.ir.179.1999, Ocean Drill. Program, College Station, Tex.

Quidelleur, X., and V. Courtillot (1996), On low-degree spherical harmonic models of paleosecular variation, *Phys. Earth Planet. Inter.*, *95*, 55–77, doi:10.1016/0031-9201(95)03115-4.

Ranero, C., and T. J. Reston (1999), Detachment faulting at ocean core complexes, *Geology*, *27*, 983–986, doi:10.1130/0091-7613(1999)027<0983:DFAOCC>2.3.CO;2.

Schouten, H., D. K. Smith, J. R. Cann, and J. Escartín (2010), Tectonic vs magmatic extension in the presence of core complexes at slow-spreading ridges from a visualization of faulted seafloor topography, *Geology*, *38*, 615–618, doi:10.1130/G30803.1.

Schroeder, T., M. J. Cheadle, H. J. B. Dick, U. Faul, J. F. Casey, and P. B. Kelemen (2007), Nonvolcanic seafloor spreading and corner-flow rotation accommodated by extensional faulting at 15°N on the Mid-Atlantic Ridge: A structural synthesis of ODP Leg 209, *Geochem. Geophys. Geosyst.*, *8*, Q06015, doi:10.1029/2006GC001567.

Sella, G. F., T. H. Dixon, and A. Mao (2002), REVEL: A model for Recent plate velocities from space geodesy, *J. Geophys. Res.*, *107*(B4), 2081, doi:10.1029/2000JB000033.

Smith, D. K., J. R. Cann, and J. Escartín (2006), Widespread active detachment faulting and core complex formation near 13°N on the Mid-Atlantic Ridge, *Nature*, *442*, 440–443, doi:10.1038/nature04950.

Smith, D. K., J. Escartín, H. Schouten, and J. R. Cann (2008), Fault rotation and core complex formation: Significant processes in seafloor formation at slow-spreading mid-ocean ridges (Mid-Atlantic Ridge, 13°–15°N), *Geochem. Geophys. Geosyst.*, *9*, Q03003, doi:10.1029/2007GC001699.

Spencer, J. E. (1999), Geologic continuous casting below continental and deep-sea detachment faults and at the striated extrusion of Sacsayhuamán, Peru, *Geology*, *27*, 327–330, doi:10.1130/0091-7613(1999)027<0327:GCCBCA>2.3.CO;2.

Toomey, D. R., S. C. Solomon, G. M. Purdy, and M. H. Murray (1985), Microearthquakes beneath the median valley of the Mid-Atlantic Ridge near 23°N: Hypocenters and focal mechanisms, *J. Geophys. Res.*, *90*, 5443–5458, doi:10.1029/JB090iB07p05443.

Tucholke, B. E., and J. Lin (1994), A geological model for the structure of ridge segments in slow spreading oceanic crust, *J. Geophys. Res.*, *99*, 11,937–11,958, doi:10.1029/94JB00338.

Tucholke, B. E., J. Lin, and M. Kleinrock (1998), Megamullions and mullion structure defining oceanic metamorphic core complexes on the Mid-Atlantic Ridge, *J. Geophys. Res.*, *103*, 9857–9866, doi:10.1029/98JB00167.

Tucholke, B. E., M. D. Behn, W. R. Buck, and J. Lin (2008), Role of melt supply in oceanic detachment faulting and formation of megamullions, *Geology*, *36*, 455–458, doi:10.1130/G24639A.1.

Wernicke, B. (1995), Low-angle normal faults and seismicity: A review, *J. Geophys. Res.*, *100*, 20,159–20,174, doi:10.1029/95JB01911.

Wernicke, B., and G. J. Axen (1988), On the role of isostasy in the evolution of normal fault systems, *Geology*, *16*, 848–851, doi:10.1130/0091-7613(1988)016<0848:OTROII>2.3.CO;2.

Yu, Y. J., D. J. Dunlop, O. Ozdemir, and H. Ueno (2001), Magnetic properties of Kurokami pumices from Mt. Sakurajima, Japan, *Earth Planet. Sci. Lett.*, *192*, 439–446, doi:10.1016/S0012-821X(01)00464-2.

Zhao, X., and M. Tominaga (2009), Paleomagnetic and rock magnetic results from lower crustal rocks of IODP Site U1309: Implication for thermal and accretion history of the Atlantis Massif, *Tectonophysics*, *474*, 435–448, doi:10.1016/j.tecto.2009.04.017.

Zhao, X., P. Riisager, M. Antretter, J. Carlut, P. Lippert, Q. Liu, B. Galbrun, S. Hall, H. Delius, and T. Kanamatsu (2006), Unraveling the magnetic carriers of igneous cores from the Atlantic, Pacific, and the southern Indian oceans with rock magnetic characterization, *Phys. Earth Planet. Inter.*, *156*, 294–328, doi:10.1016/j.pepi.2005.08.005.

Zijderveld, J. D. A. (1967), A.C. demagnetization of rocks: Analysis of results, in *Methods in Paleomagnetism*, edited by D. W. Collinson et al., pp. 254–268, Elsevier, Amsterdam.